Chemical Engineering Journal 499 (2024) 156250

Contents lists available at ScienceDirect

Chemical Engineering Journal

journal homepage: www.elsevier.com/locate/cej

Multiple defect states engineering towards high thermoelectric performance in GeTe-based materials

Taras Parashchuk [a,*], Bartlomiej Wiendlocha [b], Oleksandr Cherniushok [a], Kacper Pryga [b], Kamil Ciesielski [c], Eric Toberer [c], Krzysztof T. Wojciechowski [a,d,*]

[a] *AGH University of Krakow, Faculty of Materials Science and Ceramics, Department of Inorganic Chemistry, Thermoelectric Research Laboratory, Mickiewicza Ave. 30, 30-059 Krakow, Poland*
[b] *AGH University of Krakow, Faculty of Physics and Applied Computer Science, Mickiewicza Ave. 30, 30-059 Krakow, Poland*
[c] *Colorado School of Mines, Department of Physics, Golden 80401, CO, United States*
[d] *AGH University of Krakow, Centre of Energy, Laboratory of Thermoelectric Technologies, Mickiewicza Ave. 30, 30-059 Krakow, Poland*

ARTICLE INFO

Keywords:
GeTe
Electronic and Thermal Transport Properties
Band Convergence
Energy Conversion Efficiency

ABSTRACT

GeTe is a promising material for thermoelectric (TE) applications. However, its low Seebeck coefficient and high thermal conductivity in the mid-temperature range of 298–550 K have hindered its widespread use in TE devices. In this work, we show that a combination of band engineering, Fermi level tuning, and miscibility gap exploration can significantly improve the energy conversion performance of GeTe. Bi provides the optimized carrier concentration and induces band convergence, while Ga possibly forms a resonant state. The synergistic effects of Bi and Ga significantly improve the Seebeck coefficient from 38 μVK^{-1} for undoped GeTe to over 120 μVK^{-1} for Bi and Ga-containing materials at 298 K and provide a high power factor over a wide temperature range. Phonon scattering is strengthened by optimizing the microstructure through Pb-induced spinodal decomposition and enhanced point defect scattering due to increased dopant solubility, resulting in a very low lattice thermal conductivity of about 0.5 $Wm^{-1}K^{-1}$ at 600 K for the triple-doped samples. The maximum thermoelectric figure of merit ZT was significantly increased to 2.1 at 600 K for the $Ge_{0.87}Pb_{0.05}Bi_{0.06}Ga_{0.02}Te$ sample due to the improved power factor and reduced lattice thermal conductivity. Additionally, the average figure of merit ZT_{ave} for this sample achieved a very high value of 1.4 for $Ge_{0.87}Pb_{0.05}Bi_{0.06}Ga_{0.02}Te$ at a temperature gradient of 475 K ($T_c = 298$ K). The developed material shows great potential for use in energy conversion devices, with an estimated energy conversion efficiency exceeding 17 %.

1. Introduction

Thermoelectric (TE) materials and devices can convert waste heat directly into electricity, helping to reduce greenhouse gas emissions [1–5]. Thermoelectric technologies are also widely used in solid-state refrigeration devices, which can provide advanced cooling solutions for the automotive industry, miniature electronic devices, and medical instruments [6–8]. The energy conversion efficiency of the thermoelectric devices working at the temperature range of ΔT ($\Delta T = T_h - T_c$, where T_h and T_c are the hot-side and cold-side temperatures) is determined by the performance of the semiconductor materials at this temperature range. The parameter that can roughly evaluate the maximum energy conversion efficiency η_{max} ($\eta_{max} = \frac{\Delta T}{T_h} \frac{\sqrt{1+ZT_{ave}}-1}{\sqrt{1+ZT_{ave}}+\frac{T_c}{T_h}}$) is the average TE figure of merit ZT_{ave} ($ZT_{ave} = \frac{1}{T_h-T_c}\int_{T_c}^{T_h} ZT\cdot dT$). At the same time, the material performance can be tested using a dimensionless TE figure of merit ZT ($ZT = \frac{S^2\sigma}{\kappa}T$) where S and σ denote the Seebeck coefficient and electrical conductivity, T is the absolute temperature, κ_L and κ_e are the lattice and electronic components of the total thermal conductivity κ, respectively [9,10]. The challenging nature of preparing the high-performance TE material is connected with the interlinked transport properties. Particularly, the Seebeck coefficient, electrical conductivity, and electronic thermal conductivity are coupled through the carrier concentration and scattering mechanisms, so ideally, they should be optimized individually [3,11,12].

Germanium telluride, due to its unique set of properties, is one of the best candidates for the construction of medium-temperature (500–800

---

* Corresponding authors at: AGH University of Krakow, Faculty of Materials Science and Ceramics, Department of Inorganic Chemistry, Thermoelectric Research Laboratory, Mickiewicza Ave. 30, 30-059 Krakow, Poland (T. Parashchuk and K.T. Wojciechowski).

E-mail addresses: parashchuk@agh.edu.pl (T. Parashchuk), wojciech@agh.edu.pl (K.T. Wojciechowski).

https://doi.org/10.1016/j.cej.2024.156250
Received 17 May 2024; Received in revised form 14 September 2024; Accepted 27 September 2024

K) TE converters [13–21]. Several works show also a promise of near-room temperature applications for GeTe [22,23]. GeTe, as one of the very best performing thermoelectric materials, has also been already used for development of devices, reaching high energy conversion efficiency, up to ca. 15 % [13,15]. The problem with the undoped GeTe is the polymorphic phase transition and a very high carrier concentration n of above 10^{21} cm^{-3} [24]. The transition from the low-temperature rhombohedral structure (space group $R3m$) to the high-temperature cubic rock salt structure (space group $Fm\text{-}3m$) occurs at around 700 K enabling the drop-change transport properties at this temperature region [25,26]. The high carrier concentration originates from the strong deviation of stoichiometry toward Ge-deficient compositions, as shown in the available phase diagram of the Ge-Te system [27,28]. The deep in-band location of chemical potential provokes a low Seebeck coefficient and very high electronic thermal conductivity, which is detrimental to ZT. Also, the lattice thermal conductivity of the undoped GeTe is reported to be around 3.0 $\text{Wm}^{-1}\text{K}^{-1}$ [25], which is too high for good thermoelectric performance [29,30].

The effective optimization of the carrier concentration in GeTe can be achieved by Bi doping [15,25,31,32], while the phonon transport can be deteriorated by PbTe alloying [24,33–35]. Both impurities *via* different doping strategies have been tested and approved in GeTe for the design of high-performance thermoelectric materials [15,31,36]. Bi in place of Ge plays the role of a donor dopant effectively reducing the carrier concentration [25,32,37,38]. Additionally, Bi impurity in GeTe changes the band structure which is reflected in the enhancement of the density of states effective mass and DFT calculations results [39]. According to the pseudo-binary GeTe-PbTe phase diagram [40], the end-member compounds form a continuous solid solution at high temperatures, which undergoes spinodal decomposition (miscibility gap) at lower temperatures, with a critical point at 36 mol% PbTe and 860 K. At 673 K the miscibility gap ranges from about 3 to 90 mol% PbTe [27,40]. Consequently, Pb impurity in GeTe effectively reduces the lattice thermal conductivity due to the presence of interphase phonon scattering as well as strong point defect scattering [41]. In terms of electronic transport, Pb is not an electrically active dopant in GeTe, but the PbTe-GeTe alloy facilitates the reduction of the hole concentration due to a smaller deviation from the stochiometric composition [24]. Ga dopant in GeTe reduces the Hall carrier concentration due to filling the vacancies on the Ge sublattice and introduces a sharp hump near the Fermi level (E_F), which was described as a resonant state or deep defect state in the electronic band structure of GeTe [42–44].

Up to now, many TE studies focus on the maximum ZT while the realistic parameter determining the energy conversion efficiency of the device is the average ZT over the broad temperature range [29]. The obtaining of high transport coefficients in a wide temperature range is a big challenge [1]. One of the well-known ways to achieve this is to enhance the Seebeck coefficient using the in-gap or resonant states in the band structure of the semiconductor material [45]. These strategies have been successfully applied in many chalcogenides by different dopants, e.g. by Sn in $\beta\text{-As}_2\text{Te}_3$ [46], Bi_2Se_3 and Bi_2Te_3 [47], by Tl in PbTe [48], by In in SnTe [49,50] and PbTe [51]. In the case of GeTe, the existence of the resonant In state near the valence band maximum causes an improvement of the average power factor [29]. However, the aforementioned property enhancement is only possible if the Fermi level is close to the band edge of the in-gap level [29], or if the valence band conversion is provided by other dopants.

In this work, aiming to develop a highly efficient GeTe-based TE material, we use the combined effect of the three approaches: i) band engineering, ii) Fermi level tuning, and iii) miscibility gap exploration. In this context, we investigated the transport properties of the GeTe material co-doped with Bi, Ga, and Pb. The Bi doping in GeTe provides optimized carrier concentration, Ga further engineers the electronic structure possibly forming a resonant state in GeTe, and Pb induces a spinodal decomposition. As a result of the well-optimized carrier concentration, increased effective mass, and low lattice thermal conductivity, a significant enhancement of the average thermoelectric figure of merit ZT_{ave} and energy conversion efficiency η was achieved for the investigated GeTe-based samples.

2. Experimental details

2.1. Materials and synthesis

Samples with the nominal compositions of $\text{Ge}_{1\text{-}x\text{-}y\text{-}z}\text{Pb}_x\text{Bi}_y\text{Ga}_z\text{Te}$ ($x = 0, y = 0, z = 0$; $x = 0.05, y = 0, z = 0$; $x = 0, y = 0.06, z = 0$; $x = 0, y = 0, z = 0.02$; $x = 0.05, y = 0.06, z = 0$; $x = 0.05, y = 0.06, z = 0.01$; $x = 0.05, y = 0.06, z = 0.02$; $x = 0.05, y = 0.06, z = 0.03$; $x = 0.05, y = 0.06, z = 0.04$) were prepared by melting high purity Ge (shot, 99.999 %), Pb (shot, 99.999 %), Bi (shot, 99.99 %), Ga (shot, 99.999 %), and Te (shot, 99.999 %) in quartz containers evacuated to a residual pressure of 10^{-5} mbar. Ampoules containing the stoichiometric element mixtures were heated to 1273 K at a rate of 10 K/h and held at this temperature for 4 h. Then the furnace with the ampules was cooled down to 873 K with a rate of 10 K/h and annealed at this temperature for 100 h aiming to receive the homogenized materials. The cooling of the furnace to room temperature was carried out at a rate of 5 K/h.

2.2. Sintering

After the annealing process, the samples were ground into fine powders (a fraction smaller than 50 μm was used for sintering) by hand grinding in an agate mortar and then densified by Spark Plasma Sintering (SPS) technique at 823 K for 30 min in 12.8 mm diameter graphite dies under an axial compressive stress of 45 MPa in an argon atmosphere. The heating and cooling rate during the SPS was 100 K/min and 20 K/min, respectively. The compacted pellets with a diameter of 12.8 mm and thickness of 2 mm were obtained and polished for transport properties measurements. The density of all pellets measured by Archimedes' principle was around 97–99 % of the crystallographic density.

2.3. Powder X-ray diffraction, thermal analysis, and scanning electron microscopy

Phase identification of the prepared materials was performed with a BRUKER D8 Advance X-ray diffractometer using CuKα radiation ($\lambda = 1.5418$ Å, $\Delta 2\Theta = 0.005°$, 2Θ range $10 - 120°$) with Bragg-Brentano geometry. The lattice constants were calculated using the least square method by fitting the experimental patterns with the simulated curves. The LaB_6 XRD standard was used to improve the accuracy of the lattice constant calculations. To obtain accurate crystallographic data for the DFT calculations, we also performed Rietveld refinement of the crystal structure. The crystal structure analysis was performed using the WinCSD program package [52].

Thermal analysis of the investigated materials was performed on Differential Scanning Calorimetry equipment (NETZSCH DSC 404 F3 *Pegasus*) using a sample mass of around 12 mg in Al crucibles covered by a lid with a heating/cooling rate of 10 K/min under a helium flow.

Microstructure and chemical composition analyses were performed using scanning electron microscopy (SEM) and energy dispersive X-ray spectroscopy (EDS) on the ThermoFisher Scientific Scios 2 scanning electron microscope. For SEM and EDS analysis, the specimens were embedded in conductive resin and polished. The distribution of the Seebeck coefficient on the sample's surface was analyzed using the Scanning Thermoelectric Microscope (SThM) with a resolution of 1 μm.

2.4. Electrical and thermal transport properties

Seebeck coefficient S and electrical conductivity σ were measured with a NETZSCH SBA 458 *Nemesis*. The measurements were carried out in argon flow over the temperature range of 298——773 K. The thermal diffusivity α_D was measured on a NETZSCH LFA 457 apparatus, and the specific heat capacity C_p was estimated using the Dulong-Petit limit. Prior to measurements, all samples were spray-coated with a thin layer of graphite to minimize errors due to the emissivity of the material and laser beam reflection caused by a shiny pellet surface. The thermal conductivity was calculated using the equation $\kappa = dC_p\alpha_D$, where d is the density obtained by the Archimedes principle at the disks from SPS. The uncertainty of the Seebeck coefficient and electrical conductivity measurements was 7 and 5 %, respectively, while the uncertainty of the thermal diffusivity measurements was 3 %. The combined uncertainty for the determination of the thermoelectric figure of merit ZT is assumed to be equal to 20 % [53]. The Hall effect was investigated using Van der Pauw geometry in a custom-built apparatus [54]. We used magnetic field (0.9 T) and electrical currents from the range of 100–200 mA. The quality of ohmic contacts was checked using a voltage – current curve before measurement. The uncertainty of Hall measurements was around 10 %. The speed of sound was measured at room temperature using the Olympus Epoch 650 ultrasonic flaw detector.

2.5. Computational details

Calculations of the electronic structure were performed using the relativistic full-potential Korringa-Kohn-Rostoker method with coherent potential approximation (KKR-CPA) [55,56]. Local density approximation was employed for the crystal potential with Vosko, Wilk, Nussair parametrization [57], moreover, the calculations were also repeated using the Perdew-Burke-Ernzerhof generalized gradient potential [58] and no important changes against LDA results were noticed. About 4000 **k**-points within the irreducible Brillouin zone were used for the self-consistent cycle and 400 000 **k**-points for the density of states (DOS) and Bloch spectral density functions (BSF) calculations. Angular momentum cutoff of $l_{max} = 3$ was used, and Lloyd formula was employed to calculate the Fermi level position. Experimental crystal structure parameters were used for electronic structure calculations.

3. Results and discussions

3.1. Crystal structure and phase analyses

In this work, we aimed to obtain well-tuned transport properties over the wide temperature range for high energy conversion efficiency. To achieve this ambitious goal, several doping strategies have been applied to GeTe-based thermoelectric materials (Fig. 1a). In particular, undoped GeTe, Pb-doped GeTe, Bi-doped GeTe, Ga-doped GeTe, and Pb and Bi-co-doped GeTe were investigated as reference materials. While the main series of samples investigated in this work has the chemical composition of $Ge_{1\text{-}x\text{-}y\text{-}z}Pb_xBi_yGa_zTe$ with constant content of Pb ($x = 0.05$) and Bi ($y = 0.06$) and variable amount of Ga ($0.0 \leq x \leq 0.04$).

Fig. 1b shows the powder X-ray diffraction patterns of the $Ge_{1\text{-}x\text{-}y\text{-}z}Pb_xBi_yGa_zTe$ materials after synthesis and homogenizing annealing. The main reflections were successfully indexed using the rhombohedral structure within the space group $R3m$. However, the minor impurity reflections that belong to the elemental germanium (space group $Fd\text{-}3m$) can be also detected in the experimental patterns (marked by asterisks in Fig. 1b and Figure S1). This observation is consistent with the expected deviation in stoichiometry (Ge-deficiency) and agrees with the literature data [28]. The deviation of stoichiometry results in a large concentration of the Ge vacancies and the existence of the elemental germanium as the impurity phase [14,28].

The lattice parameters and interaxial angles of the $Ge_{1\text{-}x\text{-}y\text{-}z}Pb_xBi_yGa_zTe$ materials are shown in Fig. 1c. The lattice parameter of the undoped GeTe estimated using LaB_6 internal XRD standard equals 4.2947(1) Å, and the angle is 58.013(1)°. It can be observed that the Bi and Pb atoms in GeTe increase the lattice parameter while Ga causes some decrease in the lattice parameter. The ionic radius of Pb^{2+} is 1.19 Å, of Bi^{3+} is 1.03 Å, of Ga^{3+} is 0.62 Å, and of Ge^{2+} is 0.73 Å [59]. Consequently, such a variation of the lattice parameters with the compositional change agreed with the proposed doping strategy that the impurities of Pb, Bi, and Ga occupied Ge sites. In the case of the $Ge_{1\text{-}x\text{-}y\text{-}}$

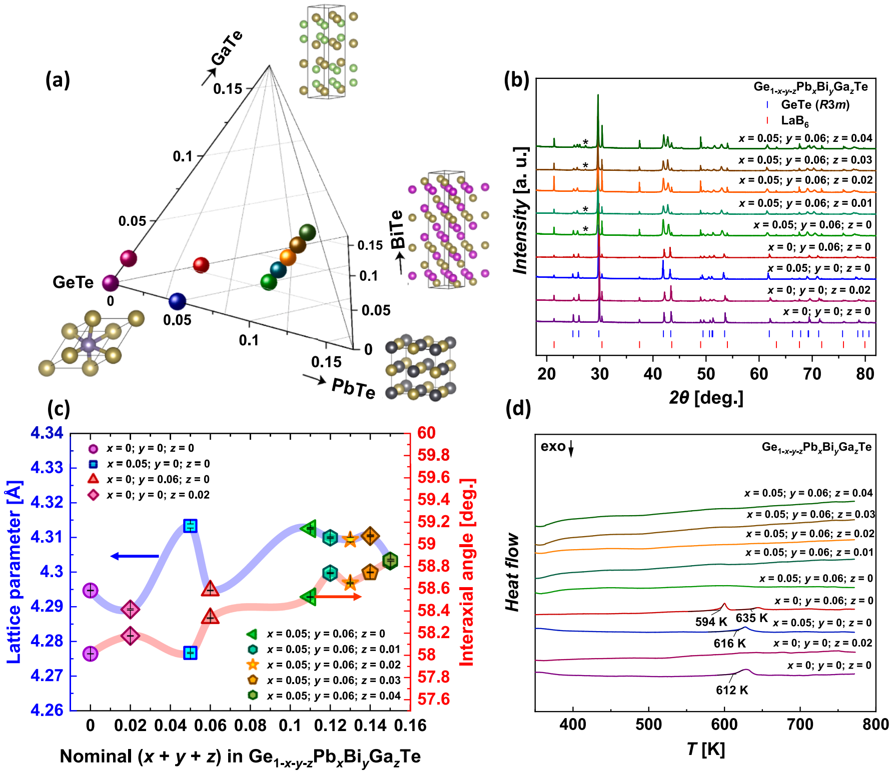

Fig. 1. (a) Studied compositions in the GeTe-PbTe-BiTe-GaTe quaternary system, (b) powder X-ray diffraction patterns, (c) lattice parameters and interaxial angles, as well as (d) DSC curves for the $Ge_{1\text{-}x\text{-}y\text{-}z}Pb_xBi_yGa_zTe$ materials.

$_{z}Pb_{x}Bi_{y}Ga_{z}Te$ materials with constant content of Pb ($x = 0.05$) and Bi ($y = 0.06$), and a variable amount of Ga ($0.0 \leq x \leq 0.04$), it can be observed a decreasing tendency of the lattice constants with the increase of z, which can also be explained by the smaller Ga^{3+} radii compared with the Ge^{2+} radii.

The thermal behavior of investigated $Ge_{1\text{-}x\text{-}y\text{-}z}Pb_{x}Bi_{y}Ga_{z}Te$ materials is presented in Fig. 1d. The DSC curve of the undoped GeTe shows a broad endothermal effect of the structural phase transition from rhombohedral to cubic starting at 612 K. The temperature of this structural phase transition strongly depends on the deviation of stoichiometry from ideal GeTe composition [27,40]. Pb doping practically does not change the temperature of polymorphic phase transition, while Bi significantly decreases this temperature. Interestingly, Ga doping practically eliminates the thermal effect of this structural transition, or this effect is smeared over a wide temperature range. The same picture was seen for all double and triple-doped $Ge_{1\text{-}x\text{-}y\text{-}z}Pb_{x}Bi_{y}Ga_{z}Te$ samples.

Fig. 2(a-j) show SEM images of the polished surfaces of $Ge_{1\text{-}x\text{-}y\text{-}z}Pb_{x}Bi_{y}Ga_{z}Te$ specimens after LFA experiments. As can be indicated from the low magnification images (Fig. 2a, c, e, g, and i), only a very minor number of pores can be found on the surface of specimens which agrees with the high densities of samples estimated using the Archimedes principle (around 97–99 % of the crystallographic density). The SEM images with higher magnification were also recorded to highlight the information about the impurity phases in the investigated samples (Fig. 2b, d, f, h, and j). The EDS analysis confirms the chemical composition of the main phase to be close to GeTe, while the nature of impurity phases was different in the case of different dopants. The common feature of almost all samples is that the black/dark regions belong to the elemental germanium precipitates. This observation is connected with the strong deviation of stoichiometry toward Ge-deficient compositions during crystallization of GeTe.

The chemical composition of the impurity phases was also identified using the EDS point analysis and EDS elemental mapping (Fig. 2 k and l). The performed experiments approved that PbTe/GeTe alloying creates the spinodal decomposing (miscibility gap) of PbTe in GeTe. This creates the submicro/nano precipitates that are mainly located in the intergrain boundaries (Fig. 2k) that may facilitate the grain boundary scattering of phonons. In turn, the doping of GeTe with Bi increases the number of Ge vacancies resulting in a larger amount of the Ge impurity phase in $Ge_{0.94}Bi_{0.06}Te$ material (Figure S2). What is also very interesting, in Fig. 2d, one can see the PbTe impurity phase, while this phase is not detected in Fig. 2j. The observation approves the increased solubility of PbTe in GeTe with the Bi and Ga dopants. The increase in the solubility of dopants is directly proportional to the increase in the number of

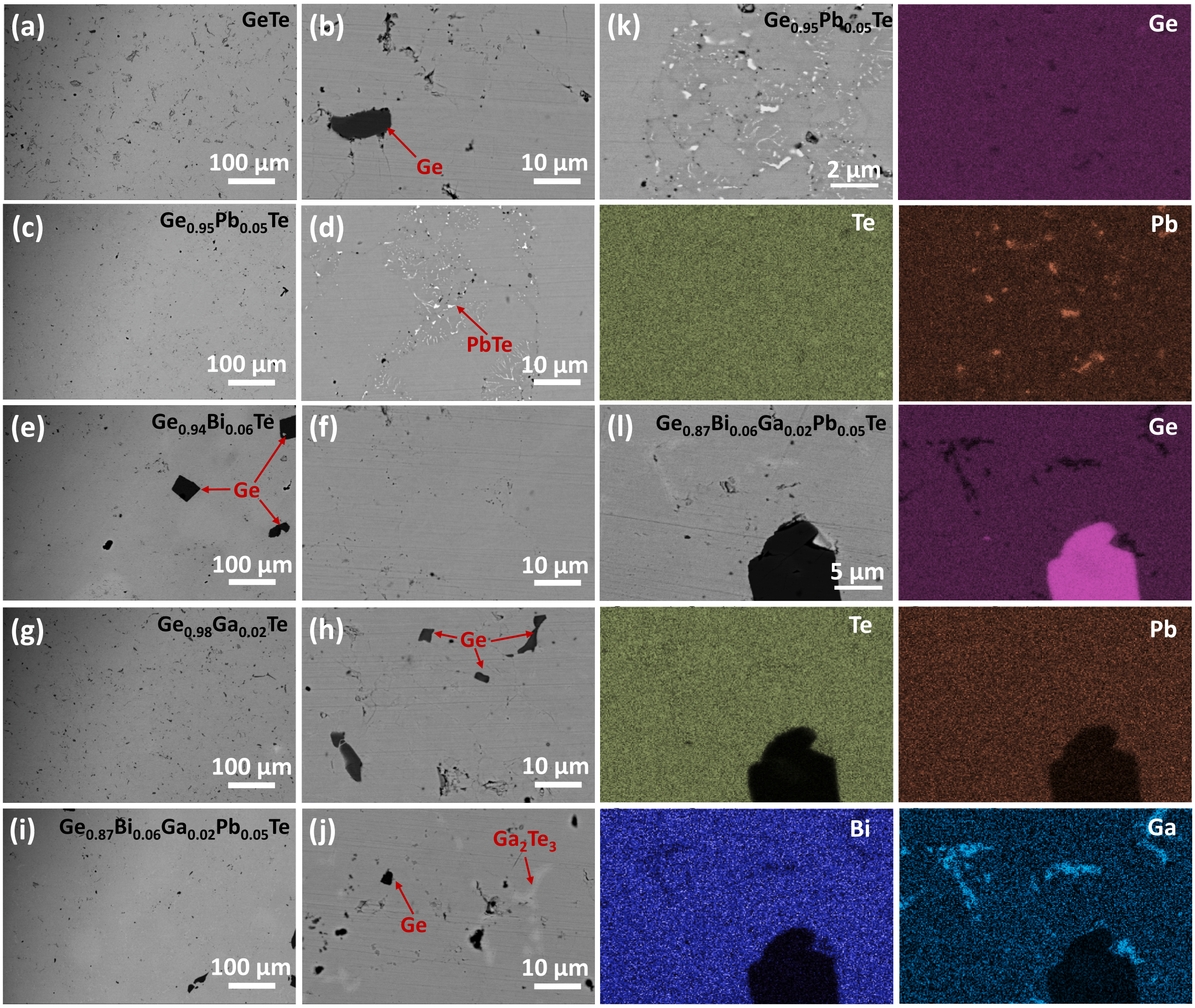

Fig. 2. SEM images of the polished surfaces of the $Ge_{1\text{-}x\text{-}y\text{-}z}Pb_{x}Bi_{y}Ga_{z}Te$ polycrystalline samples after LFA with lower (a,c,e,g,i) and higher (b,d,f,h,j) magnification: (a,b) $x = 0$; $y = 0$; $z = 0$; (c, d) $x = 0.05$; $y = 0$; $z = 0$; (e, f) $x = 0$; $y = 0.06$; $z = 0$; (g, h) $x = 0$; $y = 0$; $z = 0.02$; (i, j) $x = 0.05$; $y = 0.06$; $z = 0.02$. EDS elemental mapping images for the samples with (k) $x = 0.05$; $y = 0$; $z = 0$ and (l) $x = 0.05$; $y = 0.06$; $z = 0.02$.

dopants due to the entropy effect [2]. In particular, the increase in mixing entropy (due to the additional doping of Pb- and Bi-containing GeTe samples with Ga) leads to a negative Gibbs free energy and stabilizes a structure [60]. In such a case, we observed the increased solubility of Pb and Bi in GeTe due to the additional co-doping with Ga. This effect expands the single-phase space for performance optimization, i.e. a larger possibility for tuning the carrier concentration as well as an enhanced distortion of the lattice due to the increased point defect scattering. Similar observations have been reported in the case of Sb and Pb co-doped GeTe, where the presence of Sb increases the solubility of Pb in GeTe [41]. In Fig. 2g and j, one can also detect the presence of a Ga-rich impurity phase, which highlights the limited solubility of Ga in GeTe. In turn, the presence of Ga changes the solubility of Bi and Pb in triple-doped $Ge_{1-x-y-z}Pb_xBi_yGa_zTe$ specimens which may have a significant effect on the transport properties.

For verification of the spatial homogeneity of the investigated samples, we performed Scanning Thermoelectric Microprobe (SThM) measurements (Fig. 3a-d). Each map in Fig. 3 was plotted considering the 6400 individual measurements of the Seebeck coefficient on the polished surface of the sample. To analyze this data, the Seebeck coefficient histogram was built and fitted using the unimodal or bimodal Gaussian distribution function. The selection of the Gaussian distribution function was done considering the coefficient of determination (R^2). The analysis of all maps and Gaussian distributions for undoped GeTe (Fig. 3a), Pb-doped GeTe (Fig. 3b), Ga-doped GeTe (Fig. 3c), and triply-doped GeTe (Fig. 3d) specimens show that all samples have high spatial homogeneity compared to the other chalcogenide systems investigated in previous studies, i.e. $Pb_{1-x-y}Na_xTl_yTe$ [48], $Pb_{1-x}In_xTe_{1-y}I_y$ [51], $Bi_2Te_{3-x-y}Se_xCl_y$ [61], and $Cu_2CoSnS_{4-x}Se_x$ [62]. The average values of the Seebeck coefficient agree well with the measured Seebeck coefficients (using the Nemesis apparatus) shown in the following section. We were not able to see the impurity precipitates by SThM because the ratio of the Ge impurity phase was small (about 2 % or even less) compared with the main GeTe phase. Also, the SThM measurements in this work were performed with the step of 5 μm, which is probably too high to see the deviation in the Seebeck coefficient due to the micro-sized impurities. Somewhat lower spatial homogeneity of the Seebeck coefficient is received for the triply-doped GeTe materials, due to the largest presence of impurities in this sample. The unimodal Gaussian distribution function is the best for all GeTe-based samples, except the Pb-doped one. This can be connected with the spinodal decomposition and the existence of the PbTe-based impurity phase. However, the size of the impurity phase inclusions over the surface of the sample is too small for precise quantitative analysis.

3.2. Electronic transport properties

The electronic and thermal transport properties of the $Ge_{1-x-y-z}Pb_xBi_yGa_zTe$ materials are shown in Table 1. The Seebeck coefficient for the undoped GeTe is 34 μVK^{-1} at 298 K, which is well agreed with the previously reported values of 28–35 μVK^{-1} [13,16]. Such a relatively small S value can be explained by the very high carrier concentration n_H=1.1 × 10^{21} cm^{-3}, caused by the strong deviation of stoichiometry toward Ge-deficient compositions. The very high carrier concentration also results in a high electrical conductivity of 7816 S cm^{-1} and a high thermal conductivity of 7.9 W $m^{-1}K^{-1}$ (due to the higher electronic contributions) suggesting the need to optimize the carrier concentration.

In this work, we used electrically active Bi in place of Ge to optimize the carrier concentration. According to defect energy calculations for this system, doping of Bi on Ge is expected to produce n-type carriers, as Bi_{Ge} defect is the donor across the entire available energy space [63]. Introduction of this extrinsic substitutional defect will move the Fermi level towards the band gap. However, native GeTe is known to have a high concentration of acceptor Ge vacancy defects [63]; as such, moving the Fermi level to the right will lower the energy of Ge vacancies. Thus, we expect a doping efficiency less than 100 % with n-type Bi_{Ge} doping. Despite this native counter-dopant, we managed to reduce carrier concentration in our GeTe samples by Bi doping. As a result of the decrease of carrier concentration from 1.1 × 10^{21} cm^{-3} for undoped GeTe to 3.5 × 10^{20} cm^{-3} for 6 at.% Bi-doped GeTe (the $Ge_{1-x-y-z}Pb_xBi_yGa_zTe$ sample with $x = 0; y = 0.06; z = 0$), the Seebeck coefficient increases significantly from 34 $\mu V\ K^{-1}$ up to 83 $\mu V\ K^{-1}$. The electrical and thermal conductivities for the Bi-doped GeTe sample also drop down to the values of 1592 S cm^{-1} and 2.1 W $m^{-1}K^{-1}$, respectively. These observations show the very effective tuning of the carrier concentration due to the Bi doping.

In the cases of Pb and Ga dopants in GeTe, the effect of these dopants

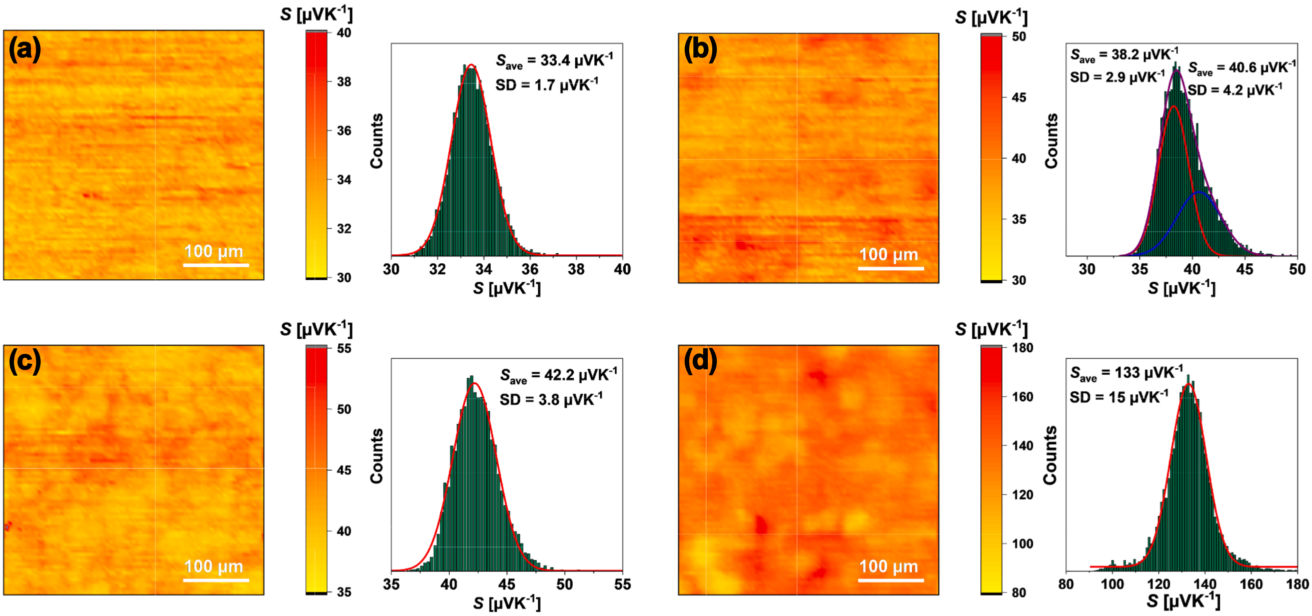

Fig. 3. SThM maps of Seebeck coefficient on the polished surfaces of the $Ge_{1-x-y-z}Pb_xBi_yGa_zTe$ polycrystalline samples: (a) $x = 0; y = 0; z = 0$; (b) $x = 0.05; y = 0; z = 0$; (c) $x = 0; y = 0; z = 0.02$; (d) $x = 0.05; y = 0.06; z = 0.02$.

Table 1
Seebeck coefficient S, electrical conductivity σ, thermal conductivity κ, Hall carrier concentration n_H, carrier mobility μ_H, and density of electronic states effective masses m^* of the $Ge_{1\text{-}x\text{-}y\text{-}z}Pb_xBi_yGa_zTe$ polycrystalline samples at 298 K.

$Ge_{1\text{-}x\text{-}y\text{-}z}Pb_xBi_yGa_zTe$	S, μV K^{-1}	σ, S cm^{-1}	κ, W m^{-1}K^{-1}	n_H, cm^{-3}	μ_H, cm^{2}V^{-1}s^{-1}	m^*/m_e
$x = 0; y = 0; z = 0$	34	7816	7.9	1.1×10^{21}	44	0.34
$x = 0.05; y = 0; z = 0$	40	6007	5.4	5.5×10^{20}	68	0.76
$x = 0; y = 0.06; z = 0$	83	1592	2.1	3.5×10^{20}	28	1.38
$x = 0; y = 0; z = 0.02$	43	6252	6.6	4.8×10^{20}	79	0.51
$x = 0.05; y = 0.06; z = 0$	119	1335	1.9	1.2×10^{20}	57	1.3
$x = 0.05; y = 0.06; z = 0.01$	129	971	1.6	1.3×10^{20}	46	1.59
$x = 0.05; y = 0.06; z = 0.02$	134	967	1.3	1.2×10^{20}	54	1.56
$x = 0.05; y = 0.06; z = 0.03$	145	733	1.2	9.1×10^{19}	50	1.55
$x = 0.05; y = 0.06; z = 0.04$	136	824	1.2	1.1×10^{20}	46	1.56

on the carrier concentration is rather weaker than in the case of Bi. Particularly, the presence of 5 at. % of Pb dopant decreases the carrier concentration to the value of 5.5×10^{20} cm^{-3} producing slightly higher Seebeck coefficient of 40 μVK^{-1} if compared to the undoped GeTe. Electrical and thermal conductivities are somewhat lower at 6007 S cm^{-1} and 5.4 W m^{-1}K^{-1}, respectively. In this case, the reduction of carrier concentration originates from the reduction of the number of Ge vacancies, as Pb itself is an isoelectronic element to Ge. Interestingly, 2 at. % of Ga in GeTe also decreases the carrier concentration, in spite of the fact that Ga is a monovalent acceptor (see [42] and the discussion below). Thus, it also has to be attributed to the reduction of the number of Ge vacancies, which are divalent *p*-type impurities.

In the case of the double and triple-doped GeTe samples, a large decrease in the carrier concentration is detected producing high values of the Seebeck coefficient (around 119–145 μVK^{-1}) and moderate electrical conductivity (824–1335 cm^{-1}) at 298 K. In turn, the total thermal conductivity κ at 298 K decreases significantly for these samples (1.2–1.9 W m^{-1}K^{-1}), as shown in Table 1.

The electronic transport in the investigated $Ge_{1\text{-}x\text{-}y\text{-}z}Pb_xBi_yGa_zTe$ materials was also analyzed using the calculated density of electronic states effective masses m^* (Table 1 and Fig. 4a). The values of m^* were estimated using the Kane band model within the procedure described in the Supporting Information. The lowest effective mass was obtained for the undoped GeTe samples, while the highest m^* is for the Bi-containing samples. This can be connected with the band convergence recently reported for the Sb-doped GeTe [64]. Bi-doped GeTe is also expected to have a similar effect. The triply-doped GeTe materials show significant enhancement of the m^* value up to $1.59m_e$.

To better visualize and analyze the changes in the effective masses, we plot the Pisarenko dependence of the Seebeck coefficient S and the carrier concentration n_H for $Ge_{1\text{-}x\text{-}y\text{-}z}Pb_xBi_yGa_zTe$ materials at 298 K (Fig. 4a). Such a dependence is very useful for understanding the electronic structure changes caused by the different doping mechanisms. In particular, the Pisarenko plot is very useful in identifying the resonant dopants [45,48]. The best fitting of the experimental data of $S(n_H)$ with the calculated curves was possible using the effective masses varied in the range of 0.5–1.5m_e. The obtained results were also compared with the literature data reported for the Pb, Bi, or Ga-doped GeTe [13,42,65].

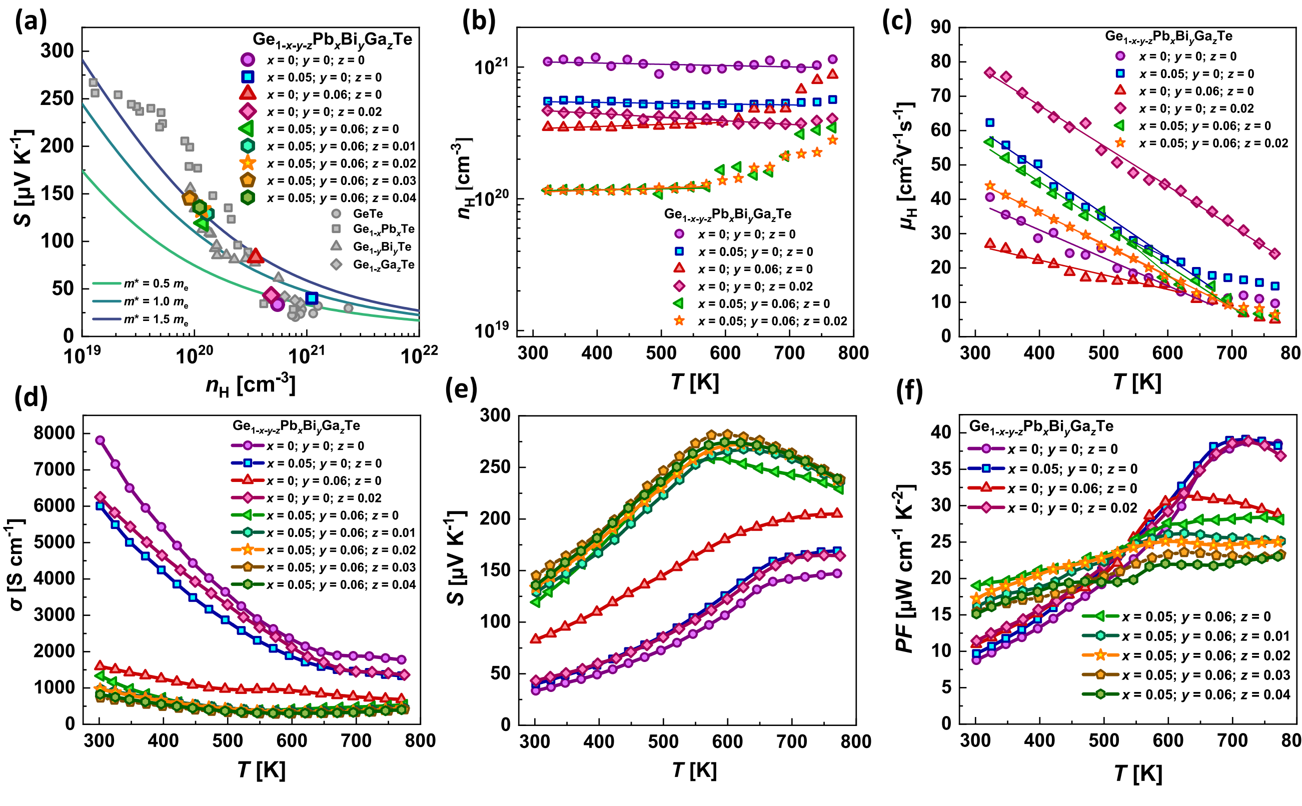

Fig. 4. (a) Pisarenko plot of the Seebeck coefficient and carrier concentration in $Ge_{1\text{-}x\text{-}y\text{-}z}Pb_xBi_yGa_zTe$ at 298 K. Solid lines were calculated within the Kane band model. Grey symbols indicate the experimental data reported for the p-type GeTe-based materials in the literature [13,42,65]. Temperature dependences of the (b) Hall concentration, (c) charge carrier mobility, (d) electrical conductivity, (e) Seebeck coefficient, and (f) Power Factor in $Ge_{1\text{-}x\text{-}y\text{-}z}Pb_xBi_yGa_zTe$ materials.

As can be seen in Fig. 4a, the obtained experimental data roughly corresponds with the literature data for most samples. At the same time, significant disagreements between our results and literature data can be found for the case of Pb-doped GeTe (grey squares at the range of low carrier concentrations in Fig. 4a). The very high effective mass (about $1.8m_e$) obtained using data from ref. [65] can be explained by the very high content of PbTe in GeTe in the samples investigated by the authors (about 40–60 at. %). The mentioned materials were prepared by quenching from a high temperature (higher than the miscibility gap temperature), resulting in the single-phase $Ge_{1-x}Pb_xTe$ solid solution. As a result, the highest possible band convergence and high effective mass were reported in the system studied by the authors [65]. In the case of our samples, we explored only up to 5 %-Pb-doped samples, and the cooling process was carried out at a rate of only 5 K/h in order to achieve the limited solubility of Pb in GeTe due to spinodal decomposition. This can be a reason for the lower effective mass in our Pb-doped GeTe samples. The Bi-containing samples (our results and literature data) show higher values of the effective mass compared to the undoped GeTe. This indicates that the Bi doping in GeTe provoke the band convergence effect. In turn, the single-Ga-doped sample does not show the clear evidence of the resonant state in GeTe. We observe a slight increase in thermopower and effective mass but the effect is not as strong as in PbTe:Tl [66] or SnTe:In [67]. It has already been noted in the literature [42,44] that the possible Ga resonant state gives more subtle effect and requires a careful tuning of the sample composition and chemical potential position for the effect to be observed. The effect of both dopants (Bi and Ga) on the electronic structure of the GeTe are discussed in the following section.

To estimate the temperature-dependent charge carrier concentration and mobility of the $Ge_{1-x-y-z}Pb_xBi_yGa_zTe$ materials, we performed the high-temperature Hall measurements (Fig. 4b). The temperature-dependent carrier concentration does not change with the temperature increase over the whole investigated temperature range for undoped, single-Pb-doped, and single-Ga-doped GeTe, which is expected for heavily degenerate semiconductors. In the case of Bi-containing materials (the samples with much lower carrier concentrations), the carrier concentration remains unchanged up to around 500 K. Above this temperature the $n_H(T)$ tendency shows a positive slope due to the activations of the intrinsic conduction mechanism.

The electrical conductivity decreases with temperature rise indicating metallic behavior for all $Ge_{1-x-y-z}Pb_xBi_yGa_zTe$ specimens (Fig. 4d). The temperature dependencies of σ for undoped, single-Pb-doped, single-Bi-doped, and single-Ga-doped GeTe specimens agree with the reported literature data [13,42,65]. The Seebeck coefficient shows positive values over the whole temperature range indicating holes as the dominant charge carriers for the investigated specimens (Fig. 4e). For undoped or single-doped samples, the Seebeck coefficient increases over the whole measured temperature range. For the undoped sample, both the Seebeck coefficient and electrical resistivity show a slight change of slope at ca. 650 K, which corresponds to the structural phase transition in GeTe. In the case of double and triply-doped GeTe materials, the Seebeck coefficient shows a maximum at around 600 K indicating the activation of the minority carrier transport. We also would like to mention the much better repeatability of properties in triply doped materials compared to the single doped ones (Figure S5).

To estimate the possible enhancement of the electronic transport properties in the developed $Ge_{1-x-y-z}Pb_xBi_yGa_zTe$ materials, we calculated the power factor ($PF=S^2\sigma$) (Fig. 4f). In the case of the undoped and single-doped GeTe materials, the temperature-dependent power factor shows a maximum of almost 40 μW $cm^{-1}K^{-2}$ at 700 K, while the room-

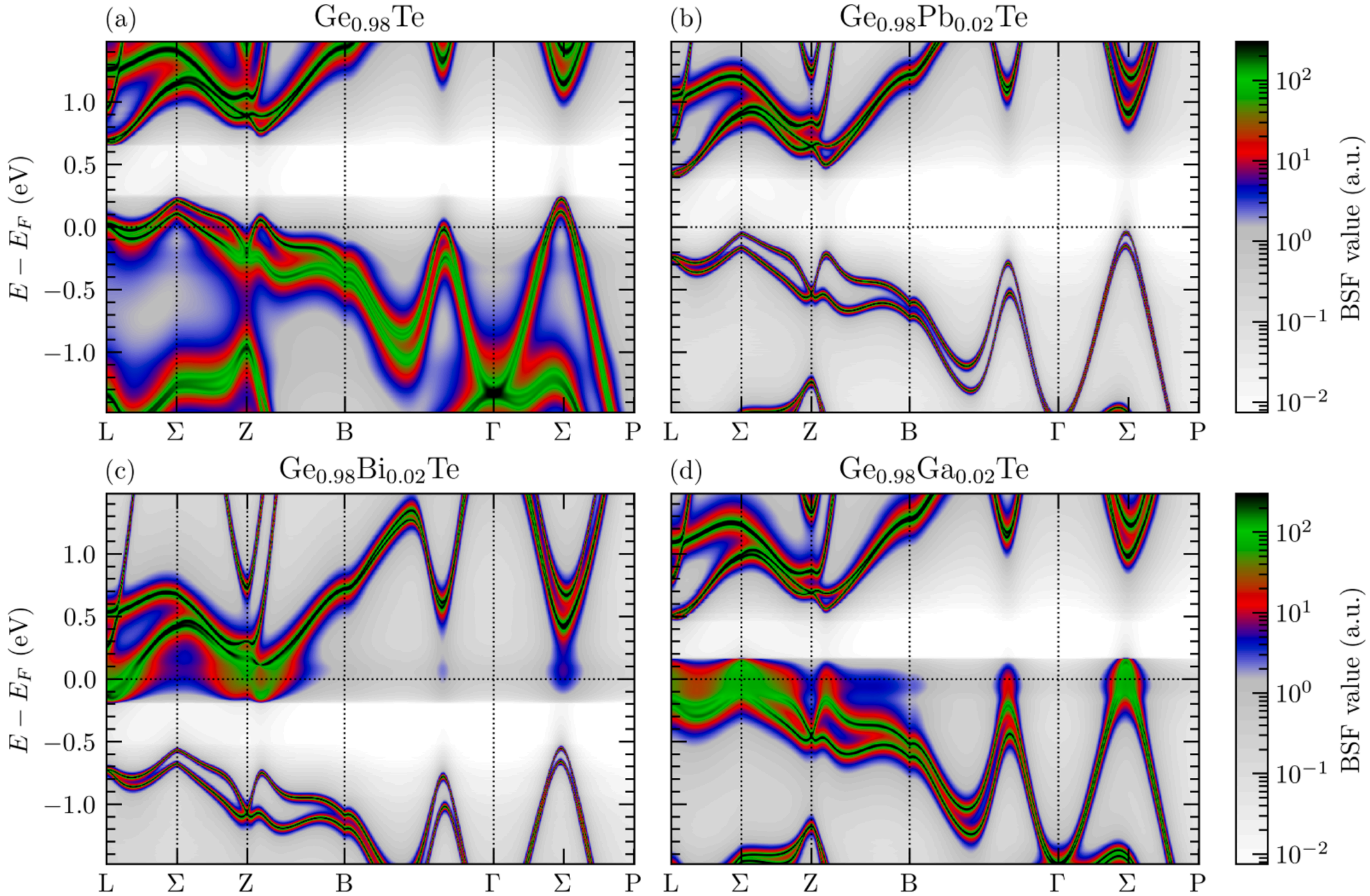

Fig. 5. Two-dimensional projections of Bloch spectral functions for GeTe: (a) containing 2% of Ge vacancies, (b) doped with 2% of Pb, (c) 2% of Bi, and (d) 2% of Ga. The value of BSF is represented by color, plotted in a logarithmic scale.

temperature *PF* is around 4 times lower (8–12 μW $cm^{-1}K^{-2}$). This results in a rather narrow bell-shaped temperature-dependent power factor in these samples. In turn, the power factor for triply doped GeTe specimens shows a much broader temperature dependence with almost 2-times higher room temperature values (15–19 μW $cm^{-1}K^{-2}$).

3.3. Calculated electronic structure

Fig. 5 shows the calculated Bloch spectral density functions (BSFs) for GeTe containing 2 % of Ge vacancies (panel a) and doped with 2 % of Pb (b), Bi (c), and Ga (d). BSFs describe the electronic dispersion relations in a disordered material, their maxima show the center of bands that are smeared due to impurity-induced electron scattering. Our calculations show the main effects of the presence of individual defects and dopant atoms on the electronic structure of GeTe. The electronic structure of pristine GeTe was discussed e.g. in [15,37,68–74] and it is consistent with our calculations. To recall its main features let us focus first on panel (b) as the presence of Pb does not lead to strong band smearing, which appears due to the presence of disorder [49,50,75,76]. The valence band maximum is located at the so-called Σ point, which is strictly speaking not a high-symmetry point but is located halfway between P and Γ (see Figure S3 in Supporting Information for the Brillouin zone with high-symmetry points). This point is the analog of the Σ point in the rock-salt PbTe or SnTe where the second valence band maximum is located (so-called “heavy” valence band, being in fact the second maximum of the L-Σ band). Here, due to the rhombohedral distortion, the band maxima are shifted, and it is the Σ point that hosts the top of the valence band. In GeTe, the band structure is additionally split by the spin–orbit interaction due to the lack of the inversion center in the rhombohedral unit cell of this polar material. The splitting of the valence band at the Σ point is about 110 meV. The next two valence band maxima are located at the L point and near the Z point (in the B-Z direction, the Z point transforms into the L point when the rhombohedral distortion disappears). These two VB maxima have energies close to each other, and their relevant position changes with doping (mostly due to changes in the details of the unit cell geometry). That makes the L-Σ-Z bands the most important for the determination of thermoelectric properties in the mid-temperature range, analogically to the L-Σ band in the sister materials PbTe and SnTe [49,77].

Moving now to the effect of impurities, in the presence of Ge vacancies (Fig. 5a) as expected the system becomes *p*-type, as each Ge vacancy delivers two holes to the material. Besides this, vacancy appears to moderately smear the band structure inducing electron scattering. In contrast, the neutral (isovalent to Ge) impurity of Pb (Fig. 5b) induces only a minor electron scattering, as the Bloch spectral functions remain sharp. That shows that Pb is an excellent impurity to be used in GeTe towards realizing Slack’s phonon glass-electron crystal idea [78], as due to a large mass difference it will effectively scatter phonons, not diminishing the mobility of electrons, or even by reducing the concentration of Ge vacancies, possibly improving the mobility at low temperatures, where the electron–phonon scattering is negligible. Apart from the effect of band smearing, both Ge vacancy and Pb do not induce strong modifications to the shape of bands and band maxima alignment. To give several characteristic numbers, the distances to the center of bands between the top of two bands at Σ and the top at L are $\Delta E_1 = 195$ meV (upper band at Σ- top at L) and $\Delta E_2 = 91$ meV (lower band at Σ – top at L) in $Ge_{0.98}Te$ while in $Ge_{0.98}Pb_{0.02}Te$ they are $\Delta E_1 = 185$ meV (upper band at Σ − top at L) and $\Delta E_2 = 75$ meV (lower band at Σ – top at L). The distances between the top at the L point and the VB maximum near Z (in the Z-B direction) are $\Delta E_3 = –35$ meV in $Ge_{0.98}Te$ and $\Delta E_3 = –25$ meV in $Ge_{0.98}Pb_{0.02}Te$ (the L point maximum is lower). Thus, in terms of the band convergence, the addition of Pb is slightly beneficial. This result also correlates with the rise of the DOS effective mass from $0.34m_e$ for undoped GeTe up to $0.76m_e$ received for the case of Pb-doped GeTe in the experimental studies (Table 1).

The third considered impurity, bismuth (Fig. 5c), is a single-electron donor, thus when only this type of impurity substitutes Ge the material would become *n*-type, with the Fermi level penetrating the conduction band. In agreement with earlier studies [29,72,79], in contrast to Pb and Ge vacancy, Bi creates stronger modifications of the shape of bands. It is possible that even a resonant-like behavior could be realized if the vacancy-free *n*-type material could be synthesized. Bi affects the conduction band mostly, visibly distorting the bands near L and Z. Importantly, in the valence band, Bi leads to increased band convergence. Shift in the valence band maxima takes place, much larger than in the case of Pb. The relevant distances between the earlier-mentioned maxima are $\Delta E_1 = 150$ meV, $\Delta E_2 = 40$ meV, and $\Delta E_3 = 30$ meV, thus L and “near-Z” maximum exchange their positions. Consequently, such a valence band convergence could be the main reason for the increase in the density of states effective mass up to $1.38m_e$ for the *p*-type single-Bi-doped GeTe material.

The last impurity of Gallium (Fig. 5d) is an acceptor and possibly creates resonant-like modifications inside the valence band [42,80]. For such a case, spectral functions near the top of valence bands are smeared, as in PbTe doped with Tl or SnTe doped with In [49,76,77,81]. Here we should also expect a stronger electron scattering at T=0 K and increased low-temperature resistivity. At room temperature the effect is not seen in our experimental studies for the Ga-doped GeTe, which has similar mobility to other samples. That may be related to the contribution of the electron–phonon scattering, being similar in all the systems, and hiding the contribution from temperature-independent resonant scattering. This again shows that the possible resonance effect from Ga is not that strong, which is consistent with the above-mentioned subtle effect on the thermopower and the effective mass and possible need for a proper optimization of the position of chemical potential. In the real Ga-doped material, the chemical potential is much deeper in the VB due to the vacancies in the structure, than in Fig. 5d, and chemical potential may not be in the optimal position. We discuss the possibility of a resonant state formation below. The calculated densities of states are shown in Fig. 6. They supplement the conclusions drawn from the analysis of the spectral functions. We can observe the strong acceptor-behavior of Ge vacancy (panel a), which moves the Fermi level deep into the valence band; the isovalent behavior of lead (panel b) with E_F not shifted by Pb; peak in the conduction band DOS formed by Bi (panel c) and peak in the valence band provided by Ga (panel d), with E_F shifted to conduction and valence bands, respectively.

Next, we have performed calculations for the case where all the impurities and Ge vacancy are present in GeTe, with the crystal structure and impurity concentrations related to the stoichiometry of the best sample studied in the experimental part, namely 5 % Pb, 6 % Bi, 2 % Ga and 2.3 % of Ge vacancies. Such a level of vacancies is needed to explain the *p*-type conductivity and the carrier concentration of $1.1 \cdot 10^{20}$ cm^{-3}. Fig. 7 shows the density of states and spectral functions. All impurities generally keep their individual character, with Ga distorting the valence band and Bi the conduction band. The Fermi level in this multi-doped material is located on a resonant-like hump in the DOS curve, which is formed due to the combined effects of band smearing and band distortions, seen in the spectral function plot. The band maxima seem also to be aligned showing increased band convergence, however here due to strong band smearing, resulting from a large amount of impurity atoms, this effect is more difficult to catch in BSF plot. In the DOS plot, on the other hand, we see a steeper DOS(E) function around E_F which explains the large DOS effective mass seen in the measurements. The combination of dopants allows us to benefit from the transport properties optimization with superimposed modifications from Ga, Pb, and Bi.

The point which we would like to discuss further is what is the mechanism behind the positive role of Ga for the thermoelectric performance of the studied series of samples and whether this comes from resonant state, possibly formed due to Ga doping, as the effect is more subtle here than in the previously studied, well-known resonant level systems as PbTe:Tl or SnTe:In [42,44,66,67]. In singly doped GeTe, the room-temperature thermopower increases from 34 to 43 μV/K, partially

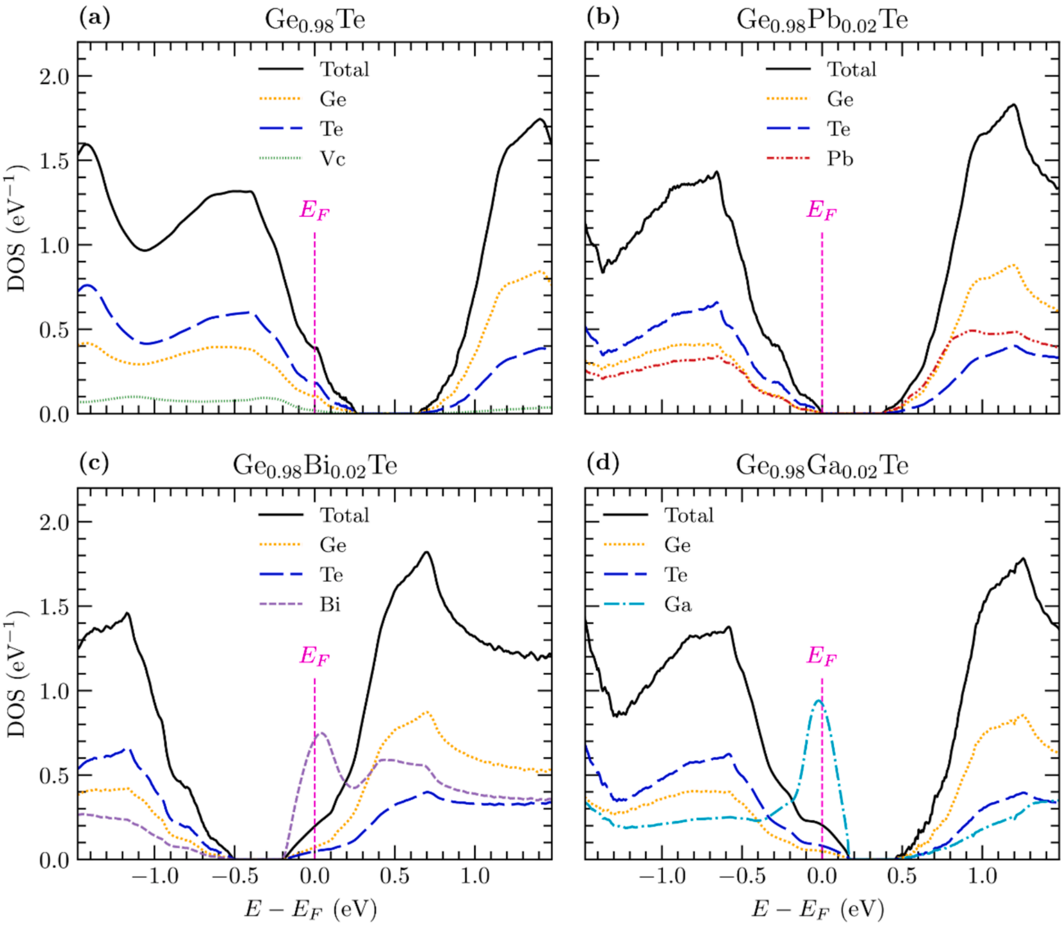

Fig. 6. Calculated density of states for GeTe: (a) containing 2% of Ge vacancies (Vc), (b) doped with 2% of Pb, (c) Bi, and (d) Ga. Partial DOS is plotted per impurity atom (not multiplied by its concentration).

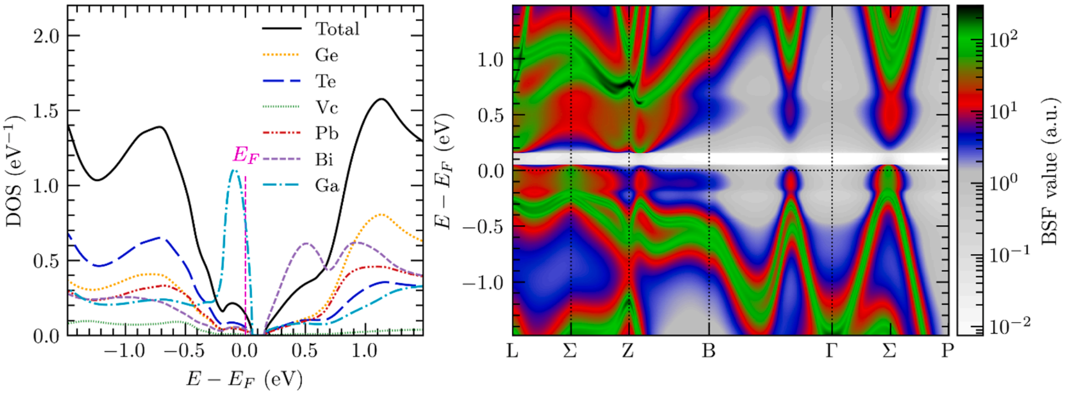

Fig. 7. (left) Density of states and (right) two-dimensional projections of Bloch spectral functions for Ge$_{0.847}$Pb$_{0.05}$Bi$_{0.06}$Ga$_{0.02}$Te. The value of BSF is represented by color, plotted in a logarithmic scale. Partial DOS is plotted per impurity atom (not multiplied by its concentration).

due to reduction of carrier concentration, but the effect is also seen on the Pisarenko curve in Fig. 4a, thus the slight increase is not only due to reduction in n_H. The effective mass increases from 0.34 to 0.51. In 5 % Pb & 6 % Bi-doped GeTe (samples have similar carrier concentrations), with increasing the Ga concentration thermopower increases from 119 to 145 μV/K and the effective mass increases from 1.3 to ~ 1.55. This, in connection with DFT calculations, suggests that the effect comes from the resonance, and we adopt this interpretation. Additionally, we have plotted the temperature-dependent mobility for the undoped ($x = 0$; $y = 0$; $z = 0$), Pb-doped, ($x = 0.05$; $y = 0$; $z = 0$), and Ga-doped ($x = 0$; $y = 0$; $z = 0.02$) GeTe samples. In Figure S4, we can see that the carrier mobility for undoped and Pb-doped GeTe samples follows the $T^{-3/2}$ dependence, indicating the dominant role of the phonon-electron scattering. For the Ga-doped sample, the large discrepancy between the theoretical $T^{-3/2}$ curve and the experimental points is seen below 450 K, that can indicate the presence of resonant scattering. Although the DFT calculations show the trace of the resonant state of Ga in GeTe, due to the complex doping scheme used in this work as well as the phase transition occurred in the material we have to be caution with concluding on the behavior of Ga. Therefore, we use the term “possible resonant state" because the true nature of Ga in GeTe is still not clear. To conclude on the resonant behavior of Ga in GeTe, low-temperature measurements of mobility should be performed, as only at low temperatures the resonant scattering effect can be proven in the absence of a strong electron–phonon scattering [50].

3.4. Thermal transport and thermoelectric performance

Fig. 8a shows the total thermal conductivity κ as a function of temperature for the.

$Ge_{1\text{-}x\text{-}y\text{-}z}Pb_xBi_yGa_zTe$ materials. The total thermal conductivity decreases with temperature until the polymorphic phase transition. At the temperature of the phase transition, the inflection of the $\kappa(T)$ is observed for all specimens. We should keep in mind that the total thermal conductivity at the high-temperature region could be affected also by the effect of bipolar conduction, which was observed in Seebeck coefficient and electrical conductivity temperature dependences.

To analyze the contribution of the lattice thermal conductivity κ_L in the total thermal conductivity κ, we estimated the electronic lattice thermal conductivity κ_e using the Wiedemann-Franz law ($\frac{\kappa_e}{\sigma} = LT$, where L is the Lorenz number). The temperature-dependent Lorenz number was calculated *via* the Kane band model approximation using the following expression [82]:

$$L_0(\eta,\beta) = \left(\frac{k_B}{e}\right)^2\left[\frac{I^2_{r+1,2}(\eta,\beta)}{I^0_{r+1,2}(\eta,\beta)} - \frac{I^1_{r+1,2}(\eta,\beta)}{I^0_{r+1,2}(\eta,\beta)}\right] \tag{1}$$

Here k_B is the Boltzmann constant, e is the charge of an electron, r is the scattering parameter, η is the reduced chemical potential, and β denotes the parameter of nonparabolicity [82]. The chemical potential and parameter of nonparabolicity were evaluated using the procedure described in the Supporting Information. The calculations were carried out within the constant relaxation time approximation, considering scattering on acoustic phonons as the main charge scattering mechanism.

The electronic contribution to the thermal conductivity is the highest for the Pb-single-doped, Ga-single-doped, and undoped GeTe samples (see Figure S7 in Supporting Information). This behavior of the electronic thermal conductivity is well aligned with the electrical conductivity temperature trends illustrated in Fig. 4d. In addition, the rest of the samples, namely the Bi-single-doped, double-doped, and triple-doped GeTe samples, exhibit considerably lower κ_e due to their markedly lower σ values.

Fig. 8b shows the calculated lattice thermal conductivity as a function of temperature over the temperature range of 298–600 K. Due to phase transitions and bipolar conduction, we do not perform calculations at higher temperatures. The estimated lattice thermal conductivity for undoped GeTe decreased from 3.1 $Wm^{-1}K^{-1}$ down to 0.8 $Wm^{-1}K^{-1}$ at the temperature range from 298 K up to 600 K, respectively. Such a temperature dependence of the κ_L is in agreement with the literature-reported range of the lattice thermal conductivity in GeTe [13,25]. The wide range of the lattice thermal conductivity in undoped GeTe is mainly related to the different grain boundary scattering, the concentration of intrinsic defects as well as the method of Lorenz number calculations. While the different temperature behavior of the lattice thermal conductivity for the Pb-single-doped GeTe samples can be attributed to a number of factors. First, Pb doping in GeTe causes spinodal decomposition, forming submicron or even nanoscale PbTe-based impurity phases (Fig. 2). These PbTe-based inclusions may be responsible for the enhanced phonon scattering observed over the mid-temperature range of 400–600 K. Another noteworthy observation is that the lower κ_L in Pb-single-doped GeTe can be attributed to its crystal

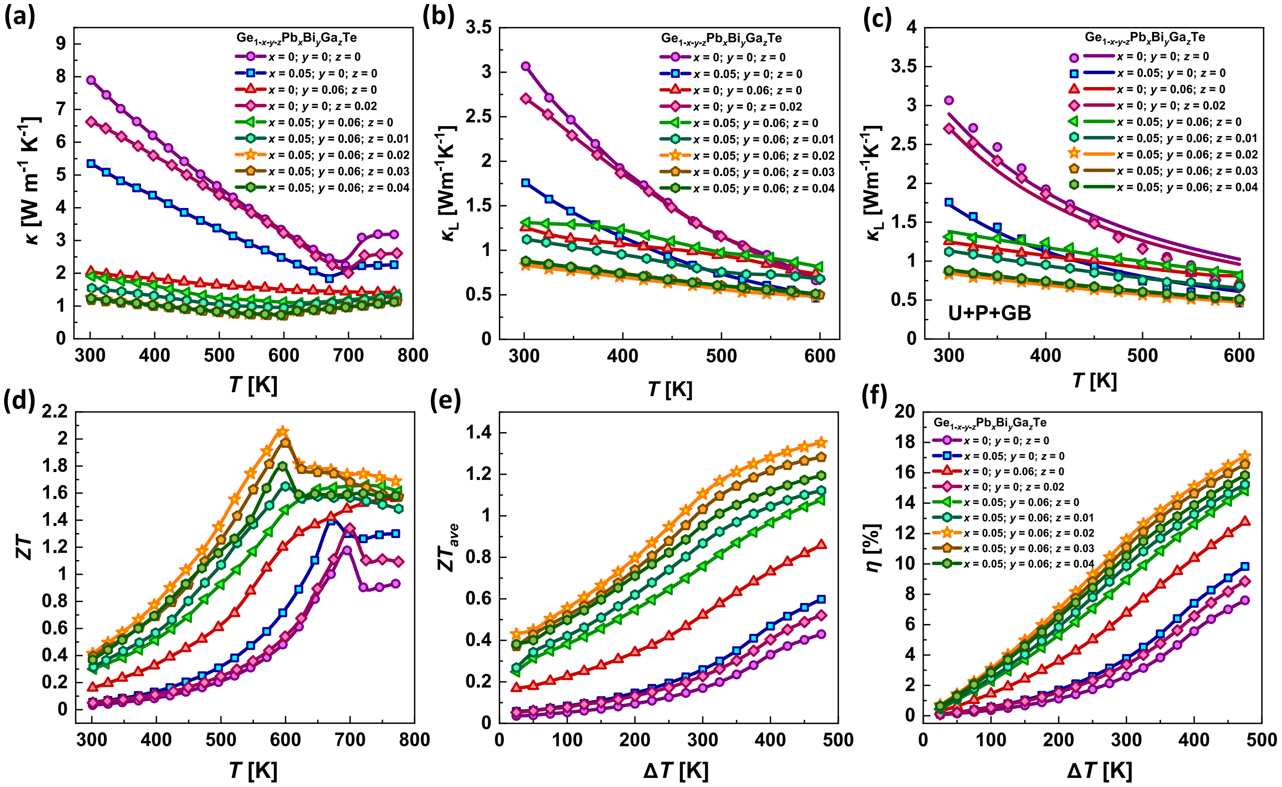

Fig. 8. Temperature dependences of (a) the total thermal conductivity, (b) lattice thermal conductivity, and (c) Callaway modeling of the lattice thermal conductivity. In panel (c) the lines correspond to the calculations using the Debye-Callaway approach, while the U, P, and GB represent Umklapp scattering, point defect scattering, and grain boundary scattering, respectively. (d) The thermoelectric dimensionless figure of merit ZT as a function of temperature. (e) Average thermoelectric figure of merit and (f) estimated energy conversion efficiency as a function of temperature gradient ΔT (ΔT=T_h-T_c, where T_h and T_c are the hot side and cold side temperature, respectively) for $Ge_{1\text{-}x\text{-}y\text{-}z}Pb_xBi_yGa_zTe$ materials.

structure. Fig. 1c shows that the Pb-doped sample's lattice parameter and the interaxial angle deviate from the trend observed in the other samples. The lattice parameter is significantly higher, while the interaxial angle is lower. Such structural distortion may be responsible for the lower κ_L. Finally, the lattice thermal conductivity was estimated using the Dulong-Petit approximation of $C_{p,}$ and the Lorenz number was evaluated using the Kane band model and the constant relaxation time approximation (with charge carrier scattering on acoustic phonons as the dominant scattering mechanism). These approximations may also be responsible for the deviation of the lattice thermal conductivity in the investigated samples.

The measured speed of sound (longitudinal v_l and transverse v_t) and calculated Debye temperatures Θ_D, the Poisson ratio ν, Grüneisen parameter γ, bulk modulus B, Young modulus E, phonon mean free path l_{ph}, and the lattice thermal conductivity κ_L for $Ge_{1-x-y-z}Pb_xBi_yGa_zTe$ materials are shown in Table 2. The Supporting Information provides details on the determination of the elastic and thermal transport properties. The average speed of sound for the investigated GeTe-based materials is in the rather narrow range of 2066–2175 m s^{-1}. Similar elastic properties indicate that the strong κ_L reduction is most likely related to change of phonon scattering in the investigated materials.

The lattice thermal conductivity of the undoped GeTe at 298 K equals 3.07 $Wm^{-1}K^{-1}$ which is in the range of the literature-reported values 2.0–5.0 $Wm^{-1}K^{-1}$ [13,25] (Table 2). The 2 at.% of Ga doping slightly decreases the κ_L to the value of 2.7 W m^{-1} K^{-1}, while 5 at.% of Pb doping and 6 at.% of Bi doping reduce the lattice thermal conductivity of GeTe significantly (to the values of 1.76 and 1.26 $Wm^{-1}K^{-1}$ at 298 K, respectively). Such a dramatic reduction of the lattice thermal conductivity for the above-mentioned samples is in line with the change of the phonon mean free path shown in Table 2 indicating the increase in the point defect concentration in these materials. In turn, we do not see a clear correlation between the Grüneisen parameter and lattice thermal conductivity suggesting rather similar phonon–phonon scattering for the investigated samples. For the triple-doped samples, the lattice thermal conductivity and phonon mean free path are around ~ 0.84–0.87 W m^{-1} K^{-1} and ~ 9.0–9.6 Å at 298 K, respectively, suggesting strong point defect scattering.

To bring some light into the origins of the low lattice thermal conductivity in the $Ge_{1-x-y-z}Pb_xBi_yGa_zTe$ materials, we performed the Debye-Callaway modeling (Fig. 8c). In this method, we performed fitting of the experimentally achieved lattice thermal conductivity with the $\kappa_L(T)$ obtained using the following expression [62,83–85]:

$$\kappa_L = \frac{k_B}{2\pi^2 v_m}\left(\frac{k_B T}{\hbar}\right)^3 \int_0^{\Theta_D/T} \tau_c(t)\frac{t^4 e^4}{(e^t-1)^2}dt \tag{2}$$

Here τ_c denotes the total phonon relaxation time, which can be expressed using Matthiessen's rule:

$$\frac{1}{\tau_c} = \frac{1}{\tau_U} + \frac{1}{\tau_P} + \frac{1}{\tau_{GB}} \tag{3}$$

where τ_U, τ_P, and τ_{GB} are the phonon relaxation time contributed from the phonon–phonon Umklapp processes scattering (U), point defect scattering (P), and grain boundary scattering (GB), respectively (Equations 4–6).

$$\tau_U^{-1} = B\left(\frac{k_B T}{\hbar}\right)^4 T^2 t^4 \tag{4}$$

$$\tau_P^{-1} = A\left(\frac{k_B T}{\hbar}\right)^4 t^4 \tag{5}$$

$$\tau_B^{-1} = \frac{\nu_m}{d} \tag{6}$$

Here $\hbar = h/(2\pi)$, $t = \hbar\omega/(k_B T)$, and d is the grain size. During the fitting procedure, the grain size d was fixed at 50 μm, while the parameters A (point-defect scattering) and B (four-phonon Umklapp scattering) were tuned to obtain the best agreement between theoretical and experimental data [62]. Consequently, information about the nature of phonon scattering for the investigated materials can be obtained from the analysis of parameters A and B [84].

In comparison with the undoped, Pb-doped, and Ga-doped GeTe specimens, a significant enhancement of the point defect scattering was observed for the Bi-doped, double-doped, and triple-doped GeTe materials (Table S1 in the Supporting Information). Because the point defect scattering in doped materials originates from the mass field and strain field fluctuations, we used the Abeles model [86] to quantify the effect of each dopant and each mechanism on the lattice thermal conductivity. Table S2 show the calculated scattering parameters $\Gamma_{calc,}$ which consist of mass field fluctuation Γ_m, and strain field fluctuation Γ_s. Supporting information contains all necessary details of the calculations. The obtained results indicate that the effect of the stain field fluctuations in about five times stronger than the mass field fluctuation for most of the materials. Due to the very similar atomic mass of Ga and Ge, the strain field fluctuations dominate significantly ($\Gamma_s/\Gamma_m = 765$) in single-Ga-doped sample, but the role of Ga in the reduction of the κ_L is rather small. The largest strain field fluctuation is coming from Pb dopant, while Bi produces the largest mass field fluctuations. The effect of Ga on the point defect scattering is very small which agrees with only minor effect of this dopant on the lattice thermal conductivity (Table S2). The effect of the phonon–phonon scattering is somewhat large for the double-doped and triple-doped GeTe specimens, while the rest samples show lower U scattering (Table S1). Consequently, the very low lattice thermal conductivity in the triple-doped series of the GeTe samples can be explained by slightly enhanced phonon–phonon scattering and significantly strengthened point defect scattering as it is derived from the Debye-Callaway analysis and ultrasonic measurements.

To evaluate the possible effect of Ge impurity phase scattering on the lattice thermal conductivity, we also performed the Debye-Callaway calculations, fixing the Umklapp scattering and opening the grain boundary scattering. In this case, however, the calculations showed a much larger discrepancy between the theoretical curves and the experimental points, suggesting that the amount of Ge impurity phases is too small to significantly affect the thermal transport properties.

Table 2
The elastic and thermal transport properties of $Ge_{1-x-y-z}Pb_xBi_yGa_zTe$ materials.

$Ge_{1-x-y-z}Pb_xBi_yGa_zTe$	v_l, m/s	v_t, m/s	v_m, m/s	Θ_D, K	ν	γ	B, GPa	E, GPa	l_{ph}, Å	κ_L, W m^{-1} K^{-1}
$x = 0; y = 0; z = 0$	3384	1959	2175	215.3	0.25	1.49	38.7	58.5	29.6	3.07
$x = 0.05; y = 0; z = 0$	3238	1868	2074	203.1	0.25	1.50	35.7	53.4	18.4	1.76
$x = 0; y = 0.06; z = 0$	3282	1849	2057	202.5	0.27	1.59	38.8	54.2	13.3	1.26
$x = 0; y = 0; z = 0.02$	3334	1939	2151	213.4	0.24	1.47	37.5	57.5	26.4	2.70
$x = 0.05; y = 0.06; z = 0$	3213	1896	2101	206.1	0.23	1.42	35.3	56.7	14.1	1.31
$x = 0.05; y = 0.06; z = 0.01$	3273	1906	2115	208.0	0.24	1.47	37.8	58.2	12.0	1.12
$x = 0.05; y = 0.06; z = 0.02$	3260	1898	2106	204.7	0.24	1.47	36.2	55.7	9.0	0.84
$x = 0.05; y = 0.06; z = 0.03$	3237	1899	2105	205.0	0.24	1.44	35.5	55.8	9.3	0.87
$x = 0.05; y = 0.06; z = 0.04$	3151	1865	2066	201.4	0.23	1.41	33.2	53.7	9.6	0.88

Fig. 8 shows the dimensionless TE figure of merit *ZT* for $Ge_{1-x-y-z}Pb_xBi_yGa_zTe$ materials at the temperature range of 298–773 K. The temperature-dependent *ZT* parameter of undoped GeTe increases with temperature, reaches a maximum value of 1.17 at 700 K, and then sharply drops down to the value of around 0.9 which could be an indicator of the phase transition from rhombohedral to cubic modification. This temperature only roughly corresponds to the thermal effect recorded at around 612 K during the DSC analysis. Such a disagreement in phase transition temperature is most probably connected with the material nature, i.e. the materials after synthesis were used for DSC analysis, while the characterization of the TE performance was done on the SPS-prepared samples. The broad range of the phase transition for undoped GeTe is also reported in the literature [13,28]. The temperature-dependent *ZT* of the other investigated materials is very similar to the undoped specimen. The difference is only in the transition temperature, i.e. with the increase of the amount of dopants the maximum in *ZT* is moved towards the low temperatures.

The *ZT* value for the undoped GeTe is low (around 0.03) at room temperature mainly due to the unoptimized carrier concentration, which agrees with the previously reported data [14,24]. In the case of Pb and Ga-doped GeTe samples, the thermoelectric figure of merit achieves the value of 0.05 suggesting rather little improvement compared to the undoped material. The much better *ZT* was obtained in the Bi-doped sample (around 0.16 at 298 K) and double-doped material (around 0.3 at 298 K) due to the tuned carrier concentration. The further optimization of the carrier concentration, low lattice thermal conductivity, and induced defect state produced the *ZT* up to 0.4 at 298 K for all triple-doped GeTe materials. Considering the maximum thermoelectric figure of merit, the undoped GeTe shows a value of 1.17, while the best sample achieves an outstanding *ZT* of around 2.1 at 600 K. This value is comparable to the best ever-reported *ZT* values for the GeTe-based alloys [13,16].

However, the maximum thermoelectric figure of merit is rather a poor indicator of good TE performance in the material [51]. To evaluate the realistic energy conversion performance of the developed materials we calculated the average *ZT* and thermoelectric efficiency η. In the case of undoped GeTe, the $ZT_{\mathrm{ave}} = 0.43$, which corresponds to the maximum achievable energy conversion efficiency of 7.6 % at the temperature gradient of 475 K ($T_c = 298$ K). In turn, thanks to the effective reduction of the lattice thermal conductivity, optimized carrier concentrations, and band engineering, which allows for the optimization of the power factor in a broad temperature range, the best ZT_{ave} reaches a much higher value of almost 1.4 at the temperature gradient of 475 K ($T_c = 298$ K), which is among the best values reported (see Figure S8 in Supporting Information) [15,20,38,87–92]. Even if each of the single-doped samples investigated in this work induce some enhancement in the estimated energy conversion efficiency (from 7.5 % for undoped GeTe up to up to 12.5 % for $Ge_{0.94}Bi_{0.06}Te$), the significant increase in η up to 17.0 % for $Ge_{0.87}Pb_{0.05}Bi_{0.06}Ga_{0.02}Te$ was possible only using the proposed multiple defects scheme (Fig. 8f). The synergy of the multiple defects is mainly represented in the increased solubility of dopants, which is one of the fundamental requirements of thermoelectric materials suggested by A. Ioffe. Consequently, the proposed multiple defect strategy opens the window for the additional carrier concentration tuning and band convergence establishment, while larger number of point defects only strength the phonon scattering and enhance the thermoelectric performance. Multiple defect states engineering was also found to be very helpful with the suppression of the phase transition in GeTe. It eliminates the effect of phase transition improving the repeatability of transport properties that is very important for device stability.

4. Conclusions

In summary, we demonstrated that the Bi, Ga, and Pb co-doped GeTe materials show great thermoelectric performance in a broad temperature range. Bi and Ga doping produces well-tuned carrier concentrations *n* and enhanced DOS effective mass *m**. Particularly, the carrier concentration is decreased from 1.11×10^{21} cm^{-3} for the undoped GeTe to 1.16×10^{20} cm^{-3} for the $Ge_{0.87}Pb_{0.05}Bi_{0.06}Ga_{0.02}Te$ while the increase of the effective mass from $0.34m_e$ to $1.56m_e$ was observed in these materials. Although Bi in place of Ge is mainly responsible for the tuning of the carrier concentration, the enhancement of the *m** values is connected with the Bi-provoked band convergence and the probably resonant hump induced by the Ga dopant. Simultaneously, by adding the isoelectronic impurities of Pb we are able to increase the mass disorder and lower the amount of Ge vacancies that helps to tune the carrier concentration and maintain a good mobility. As a result, a significant enhancement of the room-temperature Seebeck coefficient from 33.5 μVK^{-1} to 133.6 μVK^{-1} and a high power factor over the broad temperature range was achieved.

In addition to the effect of Bi and Ga-provoked defects in GeTe, the Pb-induced spinodal decomposition leads to a strong reduction of the lattice thermal conductivity from 3.07 Wm^{-1}K^{-1} for the undoped sample to 0.84 Wm^{-1}K^{-1} for $Ge_{0.87}Pb_{0.05}Bi_{0.06}Ga_{0.02}Te$ material. The beneficial effect of triple doping was also observed on their solubility, resulting in the lower presence of the impurity phases in triply co-doped GeTe samples. In addition, the thermal effect of the polymorphic phase transition observed by DSC in these samples is eliminated suggesting better repeatability of the transport properties. As a result of the synergistically improved power factor and reduced lattice thermal conductivity, the value of the best thermoelectric figure of merit reached 2.1. Due to the effectiveness of the proposed multiple defect state engineering, the average *ZT* is also enhanced significantly from 0.4 for undoped GeTe up to 1.4 for $Ge_{0.87}Pb_{0.05}Bi_{0.06}Ga_{0.02}Te$ at the same temperature gradient of 475 K ($T_c = 298$ K). The estimated energy conversion efficiency for the thermoelectric converter constructed using the developed material exceeds 17.0 %.

The combined strategy of the band engineering, Fermi level tuning, and miscibility gap exploration could be very successful in the improving *ZT* due to the synergistic effect, which is mostly reflected in the larger solubility of dopants and inhibited polymorphic phase transitions. Although the proposed strategy requires a systematic knowledge of the effect of each single dopant on the transport properties, the excellent TE performance of GeTe obtained in this work shows that the multiple defect state engineering can be successfully realized for the enhancement of thermoelectric performance in other materials.

CRediT authorship contribution statement

Taras Parashchuk: Writing – review & editing, Writing – original draft, Methodology, Investigation, Conceptualization. **Bartlomiej Wiendlocha:** Writing – review & editing, Visualization, Software, Methodology, Investigation. **Oleksandr Cherniushok:** Writing – original draft, Visualization, Methodology, Investigation, Data curation. **Kacper Pryga:** Visualization, Software, Investigation, Data curation. **Kamil Ciesielski:** Writing – review & editing, Validation, Investigation, Formal analysis. **Eric Toberer:** Writing – review & editing, Validation, Supervision, Resources. **Krzysztof T. Wojciechowski:** Validation, Resources, Project administration, Funding acquisition.

Declaration of competing interest

The authors declare that they have no known competing financial interests or personal relationships that could have appeared to influence the work reported in this paper.

Data availability

Data will be made available on request.

Acknowledgments

This work was funded by the National Science Centre (NCN) within the framework of the research projects “WEAVE-UNISONO” UMO-2022/04/Y/ST5/00139 and “OPUS-26” UMO-2023/51/B/ST11/00329. T.P. also acknowledges support from the program “Excellence Initiative - Research University” for AGH University of Krakow (IDUB AGH, grant no. 501.696.7996, Action 2, ID 4870). O.C. acknowledges support from the Foundation for Polish Science (FNP, Scholarship START program). E.S.T. and K.C. acknowledge support from NSF OAC 2118201. B.W. and K.P. acknowledge Polish high-performance computing infrastructure PLGrid (HPC Center: ACK Cyfronet AGH) for providing computer facilities and support within computational grant no. PLG/2024/017306.

Appendix A. Supplementary data

Supplementary data to this article can be found online at https://doi.org/10.1016/j.cej.2024.156250. Rietveld refinements; SEM images; Brillouin zone of GeTe with marked high-symmetry points; temperature-dependent carrier mobility; repeatability of the Seebeck coefficient and electrical conductivity; heat capacity; electronic thermal conductivity; comparison of the best thermoelectric figures of merit ZT_{ave}; details of the Kane band model calculations; details of the Lorenz number calculations; details of the elastic and thermal transport properties calculations; results of the Debye-Callaway modeling, results of the Abeles model calculations.

References

[1] Q. Yan, M.G. Kanatzidis, High-performance thermoelectrics and challenges for practical devices, Nat. Mater. 215 (21) (2021) 503–513, https://doi.org/10.1038/s41563-021-01109-w.

[2] B. Jiang, Y. Yu, J. Cui, X. Liu, L. Xie, J. Liao, Q. Zhang, Y. Huang, S. Ning, B. Jia, B. Zhu, S. Bai, L. Chen, S.J. Pennycook, J. He, High-entropy-stabilized chalcogenides with high thermoelectric performance, Science (80-.). 371 (2021) 830–834. doi: 10.1126/science.abe1292.

[3] G.J. Snyder, E.S. Toberer, Complex thermoelectric materials, Nat. Mater. 7 (2008) 105–114, https://doi.org/10.1038/nmat2090.

[4] M. Maksymuk, T. Parashchuk, A. Burbelko, K.T. Wojciechowski, Thermoelectric converter with stepwise legs for high energy conversion efficiency, Chem. Eng. J. 472 (2023) 144899, https://doi.org/10.1016/J.CEJ.2023.144899.

[5] L.I. Anatychuk, V.Y. Mykhailovsky, L.T. Strutynska, M.V. Maksymuk, V. V. Antoniuk, U. Burkhardt, W. Carrillo-Cabrera, Y. Grin, μm- and nm-Sized Catalytic Structures in Heat Sources for Thermoelectric Generators, J. Nanosci. Nanotechnol. 17 (2017) 1640–1644, https://doi.org/10.1166/jnn.2017.13720.

[6] X.L. Shi, J. Zou, Z.G. Chen, Advanced Thermoelectric Design: From Materials and Structures to Devices, Chem. Rev. 120 (2020) 7399–7515, https://doi.org/10.1021/acs.chemrev.0c00026.

[7] W.Y. Chen, X.L. Shi, J. Zou, Z.G. Chen, Thermoelectric Coolers: Progress, Challenges, and Opportunities, Small, Methods 6 (2022) 2101235, https://doi.org/10.1002/SMTD.202101235.

[8] N. Sidorenko, T. Parashchuk, M. Maksymuk, Z. Dashevsky, Development of cryogenic cooler based on n-type Bi-Sb thermoelectric and HTSC, Cryogenics (guildf). 112 (2020) 103197, https://doi.org/10.1016/J.CRYOGENICS.2020.103197.

[9] Y. Gelbstein, Z. Dashevsky, M.P. Dariel, High performance n-type PbTe-based materials for thermoelectric applications, Phys. B Condens. Matter 363 (2005) 196–205, https://doi.org/10.1016/j.physb.2005.03.022.

[10] T. Parashchuk, I. Horichok, A. Kosonowski, O. Cherniushok, P. Wyzga, G. Cempura, A. Kruk, K.T. Wojciechowski, Insight into the transport properties and enhanced thermoelectric performance of n-type $Pb_{1-x}Sb_xTe$, J. Alloys Compd. 860 (2021) 158355, https://doi.org/10.1016/J.JALLCOM.2020.158355.

[11] J. He, T.M. Tritt, Advances in thermoelectric materials research: Looking back and moving forward, Science (80-.). 357 (2017) eaak9997–eaak9997. doi: 10.1126/science.aak9997.

[12] A.F. Ioffe, L.S. Stil’bans, E.K. Iordanishvili, T.S. Stavitskaya, A. Gelbtuch, G. Vineyard, Semiconductor Thermoelements and Thermoelectric Cooling, Phys. Today 12 (1956) 42. doi: 10.1063/1.3060810.

[13] M. Hong, M. Li, Y. Wang, X.L. Shi, Z.G. Chen, Advances in Versatile GeTe Thermoelectrics from Materials to Devices, Adv. Mater. 35 (2023) 2208272, https://doi.org/10.1002/ADMA.202208272.

[14] M. Hong, Z.G. Chen, Chemistry in Advancing Thermoelectric GeTe Materials, Acc. Chem. Res. 55 (2022) 3178–3190, https://doi.org/10.1021/ACS.ACCOUNTS.2C00467.

[15] J. Li, X. Zhang, Z. Chen, S. Lin, W. Li, J. Shen, I.T. Witting, A. Faghaninia, Y. Chen, A. Jain, L. Chen, G.J. Snyder, Y. Pei, Low-Symmetry Rhombohedral GeTe Thermoelectrics, Joule 2 (2018), https://doi.org/10.1016/j.joule.2018.02.016.

[16] X. Zhang, Z. Bu, S. Lin, Z. Chen, W. Li, Y. Pei, GeTe Thermoelectrics, Joule 4 (2020) 986–1003, https://doi.org/10.1016/J.JOULE.2020.03.004.

[17] S. Zhi, J. Li, L. Hu, J. Li, N. Li, H. Wu, F. Liu, C. Zhang, W. Ao, H. Xie, X. Zhao, S. J. Pennycook, T. Zhu, Medium Entropy-Enabled High Performance Cubic GeTe Thermoelectrics, Adv. Sci. 8 (2021) 2100220, https://doi.org/10.1002/ADVS.202100220.

[18] Z. Dashevsky, I. Horichok, M. Maksymuk, A.R. Muchtar, B. Srinivasan, T. Mori, Feasibility of high performance in p-type $Ge_{1-x}Bi_xTe$ materials for thermoelectric modules, J. Am. Ceram. Soc. 105 (2022) 4500–4511, https://doi.org/10.1111/jace.18371.

[19] Q. Zhang, Z. Ti, Y. Zhu, Y. Zhang, Y. Cao, S. Li, M. Wang, D. Li, B. Zou, Y. Hou, P. Wang, G. Tang, Achieving Ultralow Lattice Thermal Conductivity and High Thermoelectric Performance in GeTe Alloys via Introducing Cu_2Te Nanocrystals and Resonant Level Doping, ACS Nano 15 (2021) 19345–19356, https://doi.org/10.1021/ACSNANO.1C05650.

[20] Q. Zhang, P. Ying, A. Farrukh, Y. Gong, J. Liu, X. Huang, D. Li, M. Wang, G. Chen, G. Tang, High wide-temperature-range thermoelectric performance in GeTe through hetero-nanostructuring, Acta Mater. 276 (2024) 120132, https://doi.org/10.1016/j.actamat.2024.120132.

[21] Y. Jiang, J. Dong, H.L. Zhuang, J. Yu, B. Su, H. Li, J. Pei, F.H. Sun, M. Zhou, H. Hu, J.W. Li, Z. Han, B.P. Zhang, T. Mori, J.F. Li, Evolution of defect structures leading to high ZT in GeTe-based thermoelectric materials, Nat. Commun. 131 (13) (2022) 1–9, https://doi.org/10.1038/s41467-022-33774-z.

[22] J. Li, Q. Hu, S. He, X. Tan, Q. Deng, Y. Zhong, F. Zhang, R. Ang, Enhancing Near-Room-Temperature GeTe Thermoelectrics through In/Pb Co-doping, ACS Appl. Mater. Interfaces 13 (2021) 37273–37279, https://doi.org/10.1021/ACSAMI.1C11599.

[23] X.Y. Tan, J.F. Dong, N. Jia, H.X. Zhang, R. Ji, A. Suwardi, Z.L. Li, Q. Zhu, J.W. Xu, Q.Y. Yan, Enhanced near-room-temperature thermoelectric performance in GeTe, Rare Met. 41 (2022) 3027–3034, https://doi.org/10.1007/S12598-022-02036-8.

[24] T. Parashchuk, A. Shabaldin, O. Cherniushok, P. Konstantinov, I. Horichok, A. Burkov, Z. Dashevsky, Origins of the enhanced thermoelectric performance for p-type $Ge_{1-x}Pb_xTe$ alloys, Phys. B Condens. Matter 596 (2020) 412397, https://doi.org/10.1016/J.PHYSB.2020.412397.

[25] Z. Liu, J. Sun, J. Mao, H. Zhu, W. Ren, J. Zhou, Z. Wang, D.J. Singh, J. Sui, C. W. Chu, Z. Ren, Phase-transition temperature suppression to achieve cubic GeTe and high thermoelectric performance by Bi and Mn codoping, Proc. Natl. Acad. Sci. u. s. a. 115 (2018) 5332–5337, https://doi.org/10.1073/PNAS.1802020115.

[26] A.A. Shabaldin, A.Y. Samunin, P.P. Konstantinov, S.V. Novikov, A.T. Burkov, Z. Bu, Y. Pei, Effect of Thermal History on the Properties of Efficient Thermoelectric Alloys $Ge_{0.86}Pb_{0.1}Bi_{0.04}Te$, Semiconductors 57 (2023) 410–414, https://doi.org/10.1134/s106378262302015x.

[27] D.K. Hohnke, H. Holloway, S. Kaiser, Phase relations and transformations in the system PbTe-GeTe, J. Phys. Chem. Solids 33 (1972) 2053–2062, https://doi.org/10.1016/S0022-3697(72)80235-X.

[28] D.I. Bletskan, Phase Equilibrium in the Systems A^{IV}—B^{VI}. Part 2. Systems Germanium—Chalcogen, ChemInform 37 (2006), https://doi.org/10.1002/CHIN.200630245.

[29] Z. Guo, G. Wu, X. Tan, R. Wang, Z. Zhang, G. Wu, Q. Zhang, J. Wu, G.-Q. Liu, J. Jiang, Z. Guo, G. Wu, X. Tan, R. Wang, Z. Zhang, Q. Zhang, J. Wu, G.-Q. Liu, J. Jiang, Enhanced Thermoelectric Performance in GeTe by Synergy of Midgap state and Band Convergence, Adv. Funct. Mater. 33 (2023) 2212421, https://doi.org/10.1002/ADFM.202212421.

[30] T. Parashchuk, O. Cherniushok, R. Cardoso-Gil, J. Tobola, Y. Grin, K.T. Wojciechowski, Discovery of the high thermoelectric performance in low-cost $Cu_8SiS_xSe_{6-x}$ argyrodites, (2023). https://arxiv.org/abs/2307.01682v1 (accessed December 28, 2023).

[31] Y. Gelbstein, J. Davidow, Highly efficient functional $Ge_xPb_{1-x}Te$ based thermoelectric alloys, Phys. Chem. Chem. Phys. 16 (2014) 20120–20126, https://doi.org/10.1039/c4cp02399d.

[32] S. Kim, S.K. Kihoi, H. Kim, J.N. Kahiu, H.S. Lee, Synergetic effect of Bi and Al co-doping in GeTe-based thermoelectric materials leading to optimized carrier concentration tuning and high ZT, J. Alloys Compd. 970 (2024) 172574, https://doi.org/10.1016/J.JALLCOM.2023.172574.

[33] H. Lian, A. Kumar, V. Ocelík, J. Baas, J. Momand, B.J. Kooi, G.R. Blake, Controlling phase separation in thermoelectric $Pb_{1-x}Ge_xTe$ to minimize thermal conductivity, J. Mater. Chem. A 9 (2021) 12340–12349, https://doi.org/10.1039/D1TA01788H.

[34] Y. Gelbstein, J. Davidow, S.N. Girard, D.Y. Chung, M. Kanatzidis, Controlling Metallurgical Phase Separation Reactions of the $Ge_{0.87}Pb_{0.13}Te$ Alloy for High Thermoelectric Performance, Adv. Energy Mater. 3 (2013) 815–820, https://doi.org/10.1002/aenm.201200970.

[35] Y. Gelbstein, J. Davidow, E. Leshem, O. Pinshow, S. Moisa, Significant lattice thermal conductivity reduction following phase separation of the highly efficient $Ge_xPb_{1-x}Te$ thermoelectric alloys, Phys. Status Solidi 251 (2014) 1431–1437, https://doi.org/10.1002/PSSB.201451088.

[36] Y. Gelbstein, B. Dado, O. Ben-Yehuda, Y. Sadia, Z. Dashevsky, M.P. Dariel, Highly efficient Ge-Rich $Ge_xPb_{1-x}Te$ thermoelectric alloys, J. Electron. Mater. 39 (2010) 2049–2052, https://doi.org/10.1007/S11664-009-1012-Z/METRICS.

[37] J. Li, Z. Chen, X. Zhang, Y. Sun, J. Yang, Y. Pei, Electronic origin of the high thermoelectric performance of GeTe among the p-type group IV monotellurides, NPG Asia Mater. 93 (9) (2017) e353, https://doi.org/10.1038/am.2017.8.

[38] T. Xing, C. Zhu, Q. Song, H. Huang, J. Xiao, D. Ren, M. Shi, P. Qiu, X. Shi, F. Xu, L. T. Chen Xing, C. Zhu, Q. Song, H. Huang, J. Xiao, D. Ren, M. Shi, P. Qiu, X. Shi,

F. Xu, L. Chen, Ultralow Lattice Thermal Conductivity and Superhigh Thermoelectric Figure-of-Merit in (Mg, Bi) Co-Doped GeTe, Adv. Mater. 33 (2021) 2008773, https://doi.org/10.1002/ADMA.202008773.

[39] Z. Guo, Q. Zhang, H. Wang, X. Tan, F. Shi, C. Xiong, N. Man, H. Hu, G. Liu, J. Jiang, Bi–Zn codoping in GeTe synergistically enhances band convergence and phonon scattering for high thermoelectric performance, J. Mater. Chem. A 8 (2020) 21642–21648, https://doi.org/10.1039/D0TA08700A.

[40] S. Gorsse, P. Bellanger, Y. Brechet, E. Sellier, A. Umarji, U. Ail, R. Decourt, Nanostructuration via solid state transformation as a strategy for improving the thermoelectric efficiency of PbTe alloys, Acta Mater. 59 (2011) 7425–7437, https://doi.org/10.1016/J.ACTAMAT.2011.07.049.

[41] J. Li, X. Zhang, X. Wang, Z. Bu, L. Zheng, B. Zhou, F. Xiong, Y. Chen, Y. Pei, High-Performance GeTe Thermoelectrics in Both Rhombohedral and Cubic Phases, J. Am. Chem. Soc. 140 (2018) 16190–16197, https://doi.org/10.1021/JACS.8B09147.

[42] B. Srinivasan, A. Gellé, F. Gucci, C. Boussard-Pledel, B. Fontaine, R. Gautier, J. F. Halet, M.J. Reece, B. Bureau, Realizing a stable high thermoelectric zT ~ 2 over a broad temperature range in $Ge_{1-x-y}Ga_xSb_yTe$ via band engineering and hybrid flash-SPS processing, Inorg. Chem. Front. 6 (2019) 63–73, https://doi.org/10.1039/C8QI00703A.

[43] C. Zhang, G. Yan, Y. Wang, X. Wu, L. Hu, F. Liu, W. Ao, O. Cojocaru-Mirédin, M. Wuttig, G.J. Snyder, Y. Yu, Grain Boundary Complexions Enable a Simultaneous Optimization of Electron and Phonon Transport Leading to High-Performance GeTe Thermoelectric Devices, Adv. Energy Mater. 13 (2023) 2203361, https://doi.org/10.1002/AENM.202203361.

[44] R. Liang, G. Yan, Y. Geng, L. Hu, F. Liu, W. Ao, C. Zhang, Compromise Design of Resonant Levels in GeTe-Based Alloys with Enhanced Thermoelectric Performance, Adv. Funct. Mater. (2024) 2404021, https://doi.org/10.1002/ADFM.202404021.

[45] J.P. Heremans, B. Wiendlocha, A.M. Chamoire, Resonant levels in bulk thermoelectric semiconductors, Energy Environ. Sci. 5 (2012) 5510–5530, https://doi.org/10.1039/c1ee02612g.

[46] B. Wiendlocha, J.-B. Vaney, C. Candolfi, A. Dauscher, B. Lenoir, J. Tobola, An Sn-induced resonant level in β-As_2Te_3, Phys. Chem. Chem. Phys. 20 (2018) 12948–12957, https://doi.org/10.1039/C8CP00431E.

[47] B. Wiendlocha, Resonant Levels, Vacancies, and Doping in Bi_2Te_3, Bi_2Te_2Se, and Bi_2Se_3 Tetradymites, J. Electron. Mater. 45 (2016) 3515–3531, https://doi.org/10.1007/s11664-016-4502-9.

[48] T. Parashchuk, B. Wiendlocha, O. Cherniushok, R. Knura, K.T. Wojciechowski, High Thermoelectric Performance of p-Type PbTe Enabled by the Synergy of Resonance Scattering and Lattice Softening, ACS Appl. Mater. Interfaces 13 (2021) 49027–49042, https://doi.org/10.1021/acsami.1c14236.

[49] S. Misra, B. Wiendlocha, J. Tobola, F. Fesquet, A. Dauscher, B. Lenoir, C. Candolfi, Band structure engineering in $Sn_{1.03}Te$ through an In-induced resonant level, J. Mater. Chem. C 8 (2020) 977–988, https://doi.org/10.1039/c9tc04407h.

[50] B. Wiendlocha, S. Misra, A. Dauscher, B. Lenoir, C. Candolfi, Residual resistivity as an independent indicator of resonant levels in semiconductors, Mater. Horizons 8 (2021) 1735–1743, https://doi.org/10.1039/d1mh00416f.

[51] K.T. Wojciechowski, T. Parashchuk, B. Wiendlocha, O. Cherniushok, Z. Dashevsky, Highly efficient n-type PbTe developed by advanced electronic structure engineering, J. Mater. Chem. C 8 (2020) 13270–13285, https://doi.org/10.1039/D0TC03067H.

[52] L. Akselrud, Y. Grin, WinCSD: Software package for crystallographic calculations (Version 4), J. Appl. Crystallogr. 47 (2014) 803–805, https://doi.org/10.1107/S1600576714001058.

[53] K.A. Borup, J. De Boor, H. Wang, F. Drymiotis, F. Gascoin, X. Shi, L. Chen, M. I. Fedorov, E. Müller, B.B. Iversen, G.J. Snyder, Measuring thermoelectric transport properties of materials, Energy Environ. Sci. 8 (2015) 423–435, https://doi.org/10.1039/c4ee01320d.

[54] K.A. Borup, E.S. Toberer, L.D. Zoltan, G. Nakatsukasa, M. Errico, J.P. Fleurial, B. B. Iversen, G.J. Snyder, Measurement of the electrical resistivity and Hall coefficient at high temperatures, Rev. Sci. Instrum. 83 (2012) 123902, https://doi.org/10.1063/1.4770124.

[55] H. Ebert, D. Ködderitzsch, J. Minár, Calculating condensed matter properties using the KKR-Green's function method - Recent developments and applications, Reports Prog. Phys. 74 (2011), https://doi.org/10.1088/0034-4885/74/9/096501.

[56] H. Ebert et al., The Munich SPR-KKR package, version 7.7 and 8.6, https://www.ebert.cup.uni-muenchen.de/index.php/en/software-en/13-sprkkr (2022) (Accessed September 30, 2024).

[57] S.H. Vosko, L. Wilk, M. Nusair, Accurate spin-dependent electron liquid correlation energies for local spin density calculations: a critical analysis, Can. J. Phys. 58 (1980) 1200–1211, https://doi.org/10.1139/p80-159.

[58] J.P. Perdew, K. Burke, M. Ernzerhof, Generalized Gradient Approximation Made Simple, Phys. Rev. Lett. 77 (1996) 3865, https://doi.org/10.1103/PhysRevLett.77.3865.

[59] R.D. Shannon, Revised effective ionic radii and systematic studies of interatomic distances in halides and chalcogenides, Acta Crystallogr. Sect. A 32 (1976) 751–767, https://doi.org/10.1107/S0567739476001551.

[60] B. Jiang, Y. Yu, H. Chen, J. Cui, X. Liu, L. Xie, J. He, Entropy engineering promotes thermoelectric performance in p-type chalcogenides, Nat. Commun. 121 (12) (2021) 1–8, https://doi.org/10.1038/s41467-021-23569-z.

[61] T. Parashchuk, R. Knura, O. Cherniushok, K.T. Wojciechowski, Ultralow Lattice Thermal Conductivity and Improved Thermoelectric Performance in Cl-Doped $Bi_2Te_{3-x}Se_x$ Alloys, ACS Appl. Mater. Interfaces 14 (2022) 33567–33579, https://doi.org/10.1021/acsami.2c08686.

[62] T. Parashchuk, O. Cherniushok, O. Smitiukh, O. Marchuk, K.T. Wojciechowski, Structure Evolution and Bonding Inhomogeneity toward High Thermoelectric Performance in $Cu_2CoSnS_{4-x}Se_x$ Materials, Chem. Mater. 35 (2023) 4772–4785, https://doi.org/10.1021/ACS.CHEMMATER.3C00586.

[63] Q. Chen, C. Yang, T. Xing, J. Xi, W. Zhang, J. Yang, L. Xi, Defect engineering and alloying strategies for tailoring thermoelectric behavior in GeTe and its alloys, J. Mater. (2024), https://doi.org/10.1016/J.JMAT.2024.01.007.

[64] T. Oku, H. Funashima, S. Kawaguchi, Y. Kubota, A. Kosuga, Superior room-temperature power factor in GeTe systems via multiple valence band convergence to a narrow energy range, Mater. Today Phys. 20 (2021) 100484, https://doi.org/10.1016/J.MTPHYS.2021.100484.

[65] Z. Bu, Z. Chen, X. Zhang, S. Lin, J. Mao, W. Li, Y. Chen, Y. Pei, Near-room-temperature rhombohedral $Ge_{1-x}Pb_xTe$ thermoelectrics, Mater. Today Phys. 15 (2020) 100260, https://doi.org/10.1016/J.MTPHYS.2020.100260.

[66] J.P. Heremans, V. Jovovic, E.S. Toberer, A. Saramat, K. Kurosaki, A. Charoenphakdee, S. Yamanaka, G.J. Snyder, Enhancement of thermoelectric efficiency in PbTe by distortion of the electronic density of states, Science 321 (2008) 554–557, https://doi.org/10.1126/science.1159725.

[67] Q. Zhang, B. Liao, Y. Lan, K. Lukas, W. Liu, K. Esfarjani, C. Opeil, D. Broido, G. Chen, Z. Ren, High thermoelectric performance by resonant dopant indium in nanostructured SnTe, Proc. Natl. Acad. Sci. u. s. a. 110 (2013) 13261–13266, https://doi.org/10.1073/PNAS.1305735110.

[68] W. Di Liu, D.Z. Wang, Q. Liu, W. Zhou, Z. Shao, Z.G. Chen, High-Performance GeTe-Based Thermoelectrics: from Materials to Devices, Adv. Energy Mater. 10 (2020) 2000367, https://doi.org/10.1002/AENM.202000367.

[69] M. Liu, J. Zhu, B. Cui, F. Guo, Z. Liu, Y. Zhu, M. Guo, Y. Sun, Q. Zhang, Y. Zhang, W. Cai, J. Sui, High-performance lead-free cubic GeTe-based thermoelectric alloy, Cell Reports Phys. Sci. 3 (2022) 100902, https://doi.org/10.1016/J.XCRP.2022.100902.

[70] G. Xing, J. Sun, Y. Li, X. Fan, W. Zheng, D.J. Singh, Thermoelectric properties of p-type cubic and rhombohedral GeTe, J. Appl. Phys. 123 (2018) 195105, https://doi.org/10.1063/1.5025070.

[71] M. Hong, Z.G. Chen, L. Yang, Y.C. Zou, M.S. Dargusch, H. Wang, J. Zou, Realizing zT of 2.3 in $Ge_{1-x-y}Sb_xIn_yTe$ via Reducing the Phase-Transition Temperature and Introducing Resonant Energy Doping, Adv. Mater. 30 (2018) 1705942, https://doi.org/10.1002/ADMA.201705942.

[72] P.C. Wei, C.X. Cai, C.R. Hsing, C.M. Wei, S.H. Yu, H.J. Wu, C.L. Chen, D.H. Wei, D. L. Nguyen, M.M.C. Chou, Y.Y. Chen, Enhancing thermoelectric performance by Fermi level tuning and thermal conductivity degradation in $(Ge_{1-x}Bi_x)Te$ crystals, Sci. Reports 91 (9) (2019) 1–6, https://doi.org/10.1038/s41598-019-45071-9.

[73] T. Wang, C. Zhang, J.Y. Yang, L. Liu, Engineering the electronic band structure and thermoelectric performance of GeTe via lattice structure manipulation from first-principles, Phys. Chem. Chem. Phys. 23 (2021) 23576–23585, https://doi.org/10.1039/D1CP03728E.

[74] D. Di Sante, P. Barone, R. Bertacco, S. Picozzi, Electric Control of the Giant Rashba Effect in Bulk GeTe, Adv. Mater. 25 (2013) 509–513, https://doi.org/10.1002/ADMA.201203199.

[75] J.S. Faulkner, G.M. Stocks, Calculating properties with the coherent-potential approximation, Phys. Rev. B 21 (1980) 3222–3244, https://doi.org/10.1103/PhysRevB.21.3222.

[76] B. Wiendlocha, Fermi surface and electron dispersion of PbTe doped with resonant Tl impurity from KKR-CPA calculations, Phys. Rev. B - Condens. Matter Mater. Phys. 88 (2013) 205205, https://doi.org/10.1103/PhysRevB.88.205205.

[77] B. Wiendlocha, Thermopower of thermoelectric materials with resonant levels: PbTe: Tl versus PbTe: Na and $_{Cu1}$-$x_N$ix, Phys. Rev. B 97 (2018) 205203, https://doi.org/10.1103/PhysRevB.97.205203.

[78] G. Slack, New Materials and Performance Limits for Thermoelectric Cooling, CRC Handb. Thermoelectr. (1995), https://doi.org/10.1201/9781420049718.ch34.

[79] S. Perumal, M. Samanta, T. Ghosh, U.S. Shenoy, A.K. Bohra, S. Bhattacharya, A. Singh, U.V. Waghmare, K. Biswas, Realization of High Thermoelectric Figure of Merit in GeTe by Complementary Co-doping of Bi and In, Joule 3 (2019) 2565–2580, https://doi.org/10.1016/J.JOULE.2019.08.017.

[80] L. Wu, X. Li, S. Wang, T. Zhang, J. Yang, W. Zhang, L. Chen, J. Yang, Resonant level-induced high thermoelectric response in indium-doped GeTe, NPG Asia Mater. 91 (9) (2017) e343, https://doi.org/10.1038/am.2016.203.

[81] S. Misra, B. Wiendlocha, J. Tobola, P. Levinský, J. Hejtmánek, S. Migot, J. Ghanbaja, A. Dauscher, B. Lenoir, C. Candolfi, Influence of In-induced resonant level on the normal-state and superconducting properties of Sn1.03Te, Phys. Rev. B 106 (2022) 075205, https://doi.org/10.1103/PHYSREVB.106.075205/FIGURES/13/MEDIUM.

[82] B.M. Askerov, Electron Transport Phenomena in Semiconductors, WORLD SCIENTIFIC (1994), https://doi.org/10.1142/1926.

[83] O. Cherniushok, R. Cardoso-Gil, T. Parashchuk, R. Knura, Y. Grin, K. T. Wojciechowski, Lone-Pair-Like Interaction and Bonding Inhomogeneity Induce Ultralow Lattice Thermal Conductivity in Filled β-Manganese-Type Phases, Chem. Mater. 34 (2022) 6389–6401, https://doi.org/10.1021/acs.chemmater.2c00915.

[84] O. Cherniushok, O.V. Smitiukh, J. Tobola, R. Knura, O.V. Marchuk, T. Parashchuk, K.T. Wojciechowski, Crystal Structure and Thermoelectric Properties of Novel Quaternary Cu2MHf3S8 (M-Mn, Fe Co, and Ni) Thiospinels with Low Thermal Conductivity, Chem. Mater. 34 (2022) 2146–2160, https://doi.org/10.1021/acs.chemmater.1c03593.

[85] J. Callaway, H.C. Von Baeyer, Effect of pint iperfections on lttice termal cnductivity, Phys. Rev. 120 (1960) 1149–1154, https://doi.org/10.1103/PhysRev.120.1149.

[86] B. Abeles, Lattice Thermal Conductivity of Disordered Semiconductor Alloys at High Temperatures, Phys. Rev. 131 (1963) 1906, https://doi.org/10.1103/PhysRev.131.1906.

[87] A. Kumar, P. Bhumla, T. Parashchuk, S. Baran, S. Bhattacharya, K. T. Wojciechowski, Engineering Electronic Structure and Lattice Dynamics to Achieve Enhanced Thermoelectric Performance of Mn–Sb Co-Doped GeTe, Chem. Mater. 33 (2021) 3620, https://doi.org/10.1021/acs.chemmater.1c00331.

[88] R.K. Vankayala, T.W. Lan, P. Parajuli, F. Liu, R. Rao, S.H. Yu, T.L. Hung, C.H. Lee, S. ichiro Yano, C.R. Hsing, D.L. Nguyen, C.L. Chen, S. Bhattacharya, K.H. Chen, M. N. Ou, O. Rancu, A.M. Rao, Y.Y. Chen, High zT and Its Origin in Sb-doped GeTe Single Crystals, Adv. Sci. 7 (2020) 2002494. doi: 10.1002/ADVS.202002494.

[89] L. Xie, Y. Chen, R. Liu, E. Song, T. Xing, T. Deng, Q. Song, J. Liu, R. Zheng, X. Gao, S. Bai, L. Chen, Stacking faults modulation for scattering optimization in GeTe-based thermoelectric materials, Nano Energy 68 (2020) 104347, https://doi.org/10.1016/J.NANOEN.2019.104347.

[90] M. Hong, W. Lyv, M. Li, S. Xu, Q. Sun, J. Zou, Z.G. Chen, Rashba Effect Maximizes Thermoelectric Performance of GeTe Derivatives, Joule 4 (2020) 2030–2043, https://doi.org/10.1016/J.JOULE.2020.07.021.

[91] M. Li, Q. Sun, S.D. Xu, M. Hong, W.Y. Lyu, J.X. Liu, Y. Wang, M. Dargusch, J. Zou, Z.G. Chen, Optimizing Electronic Quality Factor toward High-Performance $Ge_{1-x-y}Ta_xSb_yTe$ Thermoelectrics: The Role of Transition Metal Doping, Adv. Mater. 33 (2021) 2102575, https://doi.org/10.1002/ADMA.202102575.

[92] X. Zhang, J. Li, X. Wang, Z. Chen, J. Mao, Y. Chen, Y. Pei, Vacancy Manipulation for Thermoelectric Enhancements in GeTe Alloys, J. Am. Chem. Soc. 140 (2018) 15883–15888, https://doi.org/10.1021/JACS.8B09375.